Published in final edited form as:

Neuroimage. 2015 November 15; 122: 318–331. doi:10.1016/j.neuroimage.2015.08.004.

High resolution whole brain diffusion imaging at 7 T for the Human Connectome Project

AT Vu[a,1], **E Auerbach**[a], **C Lenglet**[a], **S Moeller**[a], **SN Sotiropoulos**[b], **S Jbabdi**[b], **J Andersson**[b], **E Yacoub**[a], and **K Ugurbil**[a]

[a]Center for Magnetic Resonance Research, University of Minnesota

[b]Centre for Functional Magnetic Resonance Imaging of the Brain (FMRIB), University of Oxford

Abstract

Mapping structural connectivity in healthy adults for the Human Connectome Project (HCP) benefits from high quality, high resolution, multiband (MB)-accelerated whole brain diffusion MRI (dMRI). Acquiring such data at ultrahigh fields (7 T and above) can improve intrinsic signal-to-noise ratio (SNR), but suffers from shorter T_2 and T_2* relaxation times, increased B_1^+ inhomogeneity (resulting in signal loss in cerebellar and temporal lobe regions), and increased power deposition (i.e. Specific Absorption Rate (SAR)), thereby limiting our ability to reduce the repetition time (TR). Here, we present recent developments and optimizations in 7 T image acquisitions for the HCP that allow us to efficiently obtain high-quality, high-resolution whole brain in-vivo dMRI data at 7 T. These data show spatial details typically seen only in ex-vivo studies and complement already very high quality 3 T HCP data in the same subjects. The advances are the result of intensive pilot studies aimed at mitigating the limitations of dMRI at 7 T. The data quality and methods described here are representative of the datasets that will be made freely available to the community in 2015.

INTRODUCTION

The Human Connectome Project (HCP) in the (WU-Minn) consortium, carried out as a collaboration primarily among Washington University, University of Minnesota and Oxford University, aims to generate a large, publically available database that can be used to derive descriptions of the functional and structural connections among gray matter locations in the human brain (Van Essen et al., 2013). This effort relies primarily on two magnetic resonance imaging (MRI) modalities, resting state fMRI (r-fMRI) that uses the statistical dependencies in the spontaneous temporal fluctuations in an fMRI time series to deduce ‘functional connectivity’ and diffusion weighted MRI (dMRI) for the reconstruction of the complex axonal fiber architecture so as to infer ‘structural connectivity’ between gray matter regions.

---

[1] Corresponding author: An T. Vu Ph.D., University of Minnesota Center for Magnetic, Resonance Research, Minneapolis, MN 55455, jvu@umn.edu, Phone: 612-626-6362 (office), 408-636-8375 (cell).

Two databases are being generated, one comprised of 1200 subjects with the MR data obtained on a special 3 T scanner equipped with 100 mT/m gradients and the other acquired at 7 T using 200 subjects selected from the pool of subjects scanned at 3 T. In this paper, we describe the methodological developments, parameter choices, and preliminary results for the 7 T dMRI acquisitions.

A critically important goal for the dMRI component of the HCP is to characterize the anatomical white matter connectivity patterns throughout the entire brain with as much spatial precision and accuracy as possible (Van Essen et al., 2013). Paramount to this goal is achieving higher a signal-to-noise ratio (SNR) through shorter echo times (TE) by minimizing the diffusion encoding period, and accelerating the data acquisition rate without significantly impacting SNR (i.e. increasing SNR per unit time). Higher field strengths have the potential to improve SNR in dMRI (Vaughan et al., 2001; Reischauer et al., 2012; Ugurbil et al., 2013; Ugurbil et al., 2014), but fully realizing this potential for whole brain dMRI at ultrahigh field strengths (≥7 T) is challenging due to shorter relaxation times, increased B_0 and B_1^+ (transmit B_1) inhomogeneity, and increased power deposition (Specific Absorption Rate (SAR)). While techniques do exist to mitigate these confounds to some degree, in practice, high quality, high resolution *whole brain* dMRI at high field remains challenging, especially when the acquisition times are limited to practical durations.

Recent high resolution dMRI studies at 7 T utilized partial-brain coverage (Heidemann et al., 2012; Eichner et al, 2014b; Strotmann et al., 2014), combining in-plane parallel imaging methods (Griswold et al. 1999) with outer-volume suppression (OVS), in order to minimize T_2* decay/blurring and distortion artifacts caused by B_0 inhomogeneity. The combination of these two techniques allowed a ~4-fold decrease in the echo train length, along with reductions in g-factor based SNR penalties (Pruessmann et al., 1999) compared to in-plane parallel imaging alone. However, the gain in SNR in this approach is offset by an intrinsic SNR loss due to the reduction in data sampled, proportional to the square root of the total in-plane acceleration and OVS factors applied. Additional SNR is also lost with OVS through the magnetization transfer (MT) effect, which has been shown to reduce gray/white matter signal by ~20–50% at 7 T (Pfeuffer et al., 2002). Furthermore, the addition of the OVS pulses increases both acquisition time (3 seconds per TR (Heidemann et al., 2012)) and SAR, while higher OVS factors result in smaller brain coverage (typically in the phase encoding direction). This latter point is particularly problematic since connectomic information is ideally desired over the entire brain.

Following the success of multiband (MB) acceleration (Larkman et al., 2001; Moeller et al., 2010; Setsompop et al., 2012) applied to dMRI at 3 T in the HCP (Feinberg et al., 2010; Setsompop et al., 2013; Sotiropoulos et al., 2013b; Ugurbil et al., 2013), there have been recent efforts to exploit MB acceleration for diffusion imaging at higher field strengths. The combination of MB and high field strength would allow for higher resolution, whole brain dMRI within practical scan durations. However, considering that SAR is already a concern for non-MB accelerated dMRI acquisitions at high fields, achieving even modest MB acceleration factors within SAR limits is challenging. One recent 7 T study (Eichner et al., 2014b) reduced SAR in MB-accelerated dMRI, using OVS and partial-brain coverage, by combining Variable-Rate Selective Excitation (VERSE; Conolly et al., 1988) and Power

Independent of Number of Slices (PINS; Norris et al., 2011) refocusing RF pulses. The PINS technique utilizes a spatially periodic RF pulse generated by a standard RF pulse multiplied by a Dirac comb function; its SAR is independent of the desired number of simultaneously excited slices. To keep within SAR and coil geometry/reconstruction constraints, the effective number of simultaneously excited slices is constrained by preceding the PINS refocusing pulse with a non-PINS MB VERSE excitation pulse of the corresponding desired MB acceleration factor.

The main drawback of the VERSE and PINS techniques, however, is that they typically operate with relatively low RF bandwidths and require low bandwidth-time products (BWTP) to keep RF duration and TE reasonably short. These techniques typically use a BWTP of ~2 (Eichner et al., 2014ab; while the vendor default for dMRI refocusing pulses is ~5 or higher); consequently, they are prone to having poorer slice profiles, increased slice overlap (which impacts T1 relaxation and thus SNR), and enhanced sensitivity to B_0 inhomogeneity (which can result in significant through-plane distortion and dropout in regions such as the inferior temporal and orbital frontal cortices (Gomori et al., 1988; Nagy and Weiskopf 2008; Ivanov et al., 2010)). Furthermore, all else being equal, SAR savings similar to those obtained with the use of these techniques can also be attained by simply reducing the BWTP in traditional MB dMRI for the low MB factors (2–3) typical for dMRI at 7 T (Eichner et al., 2014a). For these reasons, SAR is still a significant challenge for higher resolution, whole brain dMRI studies at 7 T, especially when MB acceleration is involved.

Due to the 3 T-7 T acquisition structure of the HCP, and the competing demands for other acquisition modalities such as r-fMRI and task-based fMRI measurements within the same scan session, the dMRI component of the HCP at 7 T is limited to 40 mins per subject in contrast to the 60 mins per subject allocated at 3 T. Thus, being able to accelerate acquisitions at 7 T, while maintaining relatively high SNR per unit time, is essential. While the techniques discussed above are potentially useful for reducing SAR and increasing temporal efficiency by going to higher slice acceleration (i.e. higher MB factors), they were eventually ruled out given the HCP's desire to achieve high quality, higher spatial resolution (~1 mm isotropic) dMRI throughout the entire brain. Instead, as part of the HCP 7 T piloting phase, we explored alternative methods to alleviate limitations imposed by SAR, real or arising due to experimental and/or instrumental imperfections, so that we could acquire high quality MB accelerated dMRI data within the limited scan time. This entailed additional challenges of combining in-plane and slice (MB) acceleration, which was not done in the 3 T HCP dMRI protocol, but is essential for high efficiency, isotropic high-resolution whole brain dMRI at 7 T. Here we present the recent advances that allow us to obtain high-quality, high resolution, whole brain dMRI data at 7 T, complementing the lower spatial, higher angular resolution data which is being collected on HCP subjects at 3 T (Figure 1). These advances are the result of two years of intensive efforts to dynamically optimize many aspects of data acquisition. The data quality described here is representative of the datasets that will be released to the community in 2015.

METHODS

Aspects of the 7 T dMRI acquisition protocol

A Siemens 7 T MAGNETOM actively shielded system (based on a 90 cm clear bore magnet) is being used as of April 2014 to scan 200 individuals selected from the subject pool included in the 1200 subject 3 T database. The scanner is equipped with a standard Siemens SC72D gradient coil with a maximum gradient amplitude (Gmax) of 70 mT/m per axis for diffusion encoding. The minimum rise time for the gradient to reach its maximum of 70 mT/m is 0.54 ms (i.e. maximum slew rate is ~125 mT/m/ms for diffusion encoding, empirically reduced due to peripheral nerve stimulation limits when using the maximum slew rate of 200 mT/m/ms for EPI imaging). This is in contrast to the custom HCP 3 T Skyra and Siemens Trio gradients which have a Gmax of 100 and 38 mT/m, respectively, and maximum slew rates of ~91 and ~62 mT/m/ms for diffusion encoding, respectively. High gradient amplitudes and slew rates are beneficial for dMRI, since they allow shortening of the diffusion encoding period as well as the image echo time (TE), and thus decreasing TR and increasing SNR per unit time. To enable concurrent in-plane and MB accelerations, a 32-channel receiver coil array with a single channel transmit coil was used (Nova Medical, Wilmington, MA).

The final acquisition protocol was determined following extensive pilot scans and evaluation of data quality, including tractography performance. Characteristics that were addressed include radio frequency (RF) pulse shapes, RF timings, partial Fourier factors, fat saturation options, phase encoding (PE) directions, monopolar and bipolar diffusion encodings, spatial resolution, multiband (MB) acceleration factors, in-plane (phase encoding) acceleration factors, gradient nonlinearities, slice excitation orders, reference scans for slice and in-plane acceleration and corresponding image reconstruction options, B_1^+ shimming options, as well as one and two shell q-space sampling schemes. Prior articles (Smith et al., 2013; Sotiropoulos et al., 2013b; Ugurbil et al., 2013) discuss additional issues regarding pulse sequence and data acquisition for both the WU-Minn HCP 3 T diffusion and functional MRI protocols.

Imaging Acceleration—As with the 3 T HCP diffusion protocol (Sotiropoulos et al., 2013b), MB acceleration is highly desirable at 7 T, particularly given the increased number of imaging slices required (>128) to cover the whole brain at higher isotropic spatial resolution. However, while longer T_2* at 3 T permitted the HCP 3 T protocol to forgo in-plane accelerations for higher SNR, for the resolutions desired at 7 T, in-plane undersampling (Griswold et al. 1999) was essential. Thus, unlike the 3 T HCP dMRI protocol, two-dimensional (2D) acceleration, along slice and phase encode directions, were employed for whole brain dMRI at 7 T. With the 32-channel coil used, in terms of image quality, blurring, and SNR (gained from the shorter attainable TE), the phase encoding direction acceleration factor of 3 (referred to as integrated-Parallel Acquisition-Techniques or iPAT factor in Siemens terminology) was found to be optimal when simultaneously using slice acceleration with MB factor of 2. A 2D (MB × iPAT) total acceleration factor of 6 (2×3) reduced the TR of a typical 1 mm, iPAT=3 only protocol from 14000 ms to an acceptable value of 7000 ms. This TR is only 27% longer than the 5500 ms TR used for the

3 T HCP diffusion protocol, even though the nominal voxel volume was reduced by 41% (over a similar whole brain imaging volume) relative to the 3 T HCP protocol. Increasing the MB factor to 3 or 4 would have permitted a more optimal TR and SNR per unit time. However, preliminary experiments found that image quality was at the limit of the 32-channel receiver coil employed, when using a 2D acceleration factor of 9 at these spatial resolutions; in addition, SAR limits would have precluded the shorter TRs. It was therefore decided to use a total 2D acceleration factor of 6 (MB=2, iPAT=3).

In-plane acceleration was also important because, unlike on the custom HCP 3 T system, we could not take advantage of a smaller phase FOV by phase encoding along the right-left (R/L) direction. This was in part due to R/L peripheral nerve stimulation limits on the 7 T system at the desired resolution, which significantly increased the minimum R/L echo spacing relative to what was achievable with an anterior-posterior (A/P) phase encoding direction. This resulted in comparable echo train lengths, even though the number of phase encoding steps with R/L phase encoding was about 15% fewer than with A/P phase encoding. Furthermore, preliminary testing revealed that acceleration performance (e.g. residual aliasing) was noticeably worse with a R/L phase encode, presumably due to the smaller number of coil elements effectively contributing to spatial encoding along the R/L direction in the Nova 32-channel coil.

Fat Saturation—To minimize both SAR as well as signal dropout due to B_0 inhomogeneity, a number of studies have found it fruitful to focus on improving the efficiency of fat saturation techniques in the context of dMRI (Nagy and Weiskopf 2008; Ivanov et al., 2010; Heidemann et al., 2012; Vu et al., 2014). One of the more common methods for fat suppression in dMRI uses a spectrally selective fat-saturation RF pulse followed by crusher gradients applied prior to the main RF excitation pulse (Rosen et al., 1984; Keller et al., 1987). This fat-suppression method requires additional RF and gradient pulses, thus increasing acquisition time as well as SAR (by ~15% for the 7 T dMRI protocol presented here). To avoid these drawbacks in the context of spin echo type sequences like dMRI, the gradient reversal technique can be used (Park et al., 1987; Gomori et al., 1988; Nagy and Weiskopf 2008). By reversing the polarity of the slice select gradient of the refocusing pulse, relative to that of the excitation pulse, chemically shifted fat signal is distorted in opposite directions and, thus, not refocused. This technique works particularly well at lower field strengths and is currently used in the HCP 3 T dMRI protocol (Sotiropoulos et al., 2013b). At higher field strengths, however, off-resonances due to B_0 inhomogeneity can be similar in magnitude to the fat-water chemical shift, resulting in signal dropout in regions like the orbito-frontal and ventral temporal lobes when the gradient reversal technique is used (Figure 2B). Rather than distorting fat in completely opposite directions, distorting it by different amounts in the same direction has been shown to effectively suppress fat with reduced sensitivity to B_0 inhomogeneity (Ivanov et al., 2010; Figure 2C). This simple low SAR technique, piloted and now being used in the HCP 7 T dMRI protocol, is achieved by setting the bandwidth of the excitation RF pulse to twice that of the refocusing pulse (through use of shorter excitation and longer refocusing pulse durations). In this way, SAR remains relatively low, since SAR is inversely proportional to RF duration, but quadratically proportional to flip angle. Since this bandwidth relationship between the excitation and refocusing pulses was also a requirement of the time-shifted MB pulse strategy employed in the 7 T HCP acquisition sequence (discussed below) the fat suppression was automatically achieved according to the principle described by (Ivanov et al., 2010).

SAR measurement error with MB pulses—As MB factors, resolution, and brain coverage increase, so do the temporal frequency modulations in the MB RF pulses (Figure 3A shows a typical MB3 example). To online SAR monitoring systems that have relatively slow impulse response functions, such rapidly modulated RF pulses can appear to maintain high voltage values (Figure 3B), resulting in erroneous online global SAR measurements that are substantially higher than what is actually being delivered. In practice, this causes scan protocols to be artificially limited to ~60–70% of the FDA SAR limit to avoid premature aborting during the scan. Recent methods originally designed for peak power reduction (Phase optimized (Wong 2012) and time-shifted MB RF pulses (Auerbach et al., 2013)), however, provide a remedy for this problem because in addition to decreasing peak power, they decrease the temporal frequency modulations in MB RF pulses. Consequently, these pulses circumvent the artificial limitation imposed by SAR measurement errors while maintaining the same RF pulse bandwidth and without significantly impacting TR or image quality. This in turn allowed MB acceleration to be more fully exploited.

The impulse response function of the online SAR monitor used for 7 T HCP acquisitions was empirically characterized as an exponential decay with a time constant of 25 μs (based on comparisons of the measured 10 second average forward power and the pre-calculated expected forward power reported in the system log files). We then compared the original excitation RF pulses (for several MB factors and slice spacings) to versions filtered by the observed impulse response function of our system. The SAR measurement Error Factor (EF) was calculated as the ratio of filtered to original RF pulse power integrals.

We found that the SAR EF increased sub-linearly with increasing slice spacing (Figure 3C) and linearly with increasing MB factor (Figure 3D) to values of up to 2–3. With the use of time-shifted MB pulses (Auerbach et al., 2013) in the HCP 7 T dMRI protocol, we were able to reduce the EF from ~1.5 to ~1.1 and decrease the overall acquisition time from 60 to 40 mins. Phase optimization (Wong 2012), which can be incorporated into the time-shifted pulses (Auerbach et al., 2013), was not employed since it had no effect on either SAR EF or peak power for MB < 3. It is important to note that the duration of time-shifting is critical and must be optimized per protocol (in Figure 3C: time-shift1=1280 μs; time-shift2=1520 μs). In our simulations, the RF duration for time-shifted pulses was defined as 5120 μs + time-shift × (MB factor – 1).

Importantly, the aligned-TE variant of time-shifting (Auerbach et al., 2013), currently employed in our dMRI protocol, ensures that the TE-induced contrast is the same across MB slices. Furthermore, because this variant of time-shifting requires that the bandwidth of the excitation pulse be twice that of the refocusing pulse, no additional fat saturation is required (Ivanov et al., 2010). This is critical for keeping both SAR and imaging time to a minimum.

Motion sensitivity in reference scan—For slice and in-plane accelerated parallel imaging, the most detrimental motion effects arise from motion during the reference scan (Ugurbil et al., 2013). If such motion effects are absent, the small motions that can occur during diffusion imaging can be corrected by post-processing approaches (Andersson et al., 2003; Andersson & Sotiropoulos, 2015ab; Sotiropoulos et al., 2013b). As mentioned previously, acquiring high isotropic resolution over the whole brain using 2D EPI requires acceleration along both the in-plane phase encoding and slice directions. The reference scans for the in-plane acceleration are typically acquired using multi-shot EPI, segmented along the phase encoding direction; such segmented acquisitions are easily degraded in the presence of motion (Moeller et al., 2010). The problem is compounded when the reference scans become very long (~30–120 sec; e.g. when high resolution is sought and/or when both in-plane and slice accelerations are used). Previous work has shown that alternative reference scans can reduce motion sensitivity in low resolution (e.g. 3 mm) in-plane accelerated 2D EPI (Griswold et al., 2006; Polimeni et al., 2015; Talagala et al., 2013; Ugurbil et al., 2013). We found similar advantages when using the GRE FLASH reference scan in the context of high-resolution slice and in-plane accelerated 2D GE and SE EPI.

To more thoroughly evaluate the advantages of the GRE reference scan, high spatial resolution whole brain gradient-echo EPI was acquired at 1.5, 1.25 and 0.9 mm^3 isotropic resolutions on an experienced subject instructed to keep still. For repeatability testing, each resolution was acquired three times per reference scan type: SEG (standard segmented EPI), SS (single shot EPI), GRE (GRE FLASH) reference. These reference scans were used for in-plane unaliasing while single-band in-plane under-sampled EPI scans were used for MB slice unaliasing. The GRE reference used here had the same readout bandwidth and ramp sampling as the EPI images, but TE and TR were minimized. Concurrent in-plane and slice acceleration factors of 3 were tested, with a 1/4 FOV shift in the phase encoding (PE) direction using blipped-CAIPIRINHA (Breuer et al., 2005; Setsompop et al., 2012). Echo spacings were minimized and TE was ~19 ms requiring 7/8, 6/8, and 5/8 partial Fourier and 1.3, 1.9, and 3.6 s TR for each resolution, respectively. Z-coverage was ~135 mm. For the 0.9 mm data, this required 150 slices and significant custom modification to both pulse sequence and reconstruction code to overcome the vendor specific 128-slice limit.

We found that the importance of the GRE reference scan increased with spatial resolution. Both ghosting and reconstruction noise levels decreased most significantly for the 0.9 mm resolution acquisition but less so for the 1.5 mm acquisition (not shown), relative to what was achieved using the standard SEG reference scan (Figure 4A). Reference scan acquisition time was not the only factor in improving image quality, however, since the shortest SS reference scan performed the poorest in terms of ghosting and noise across the three resolutions tested. The poor performance of the SS reference scan is likely due to the factor of three difference in time between echoes (echo spacing) between corresponding k-space lines of the reference scan and those of the actual under-sampled data. The results were quantified by SNR (Figure 4B) showing an improvement of up to 40% in the 0.9 mm acquisition. These improvements are expected to be larger when scanning subjects who may have more difficulty keeping still during the reference scan.

Prior studies reported that in-plane acceleration artifacts tend to appear primarily when there is relatively large head motion during the reference scan (Polimeni et al., 2015; Ugurbil et al., 2013). However, at higher spatial resolutions, such as in the HCP 7 T dMRI, a reference scan more robust to motion, like a GRE FLASH, is required for optimal image quality and SNR even with experienced still subjects. Alternative motion robust reference scans, such as FLEET (Polimeni et al., 2015) may provide further improvements, for example, due to better matching of B_0 distortions between reference and accelerated acquisitions. This is currently under evaluation but will not impact the current HCP 7 T protocol. A comparison of FLEET to the GRE reference scan was recently provided (Polimeni et al., 2015); however, the implementation of the GRE reference scan in this work was suboptimal because it did not match the readout bandwidth and ramp sampling of the MB EPI acquisition. In our implementation, this matching was done in order to minimize differences between the reference scan and the accelerated acquisition. Note, when slice acceleration is used alone (without in-plane acceleration), a single-band GRE reference scan is not necessary (Ugurbil et al., 2013).

B_1^+ inhomogeneity—With B_1^+ inhomogeneity increasing with field strength, methods to reduce such inhomogeneity become important at 7 T, especially for B_1^+ sensitive acquisitions such as SE-based dMRI. Advanced parallel transmit (pTx) Multiband pulse design techniques hold promise for dealing with this problem in MB based SE acquisitions for whole brain dMRI with simultaneous control of parameters of power deposition (Wu et al., 2013; Wu et al., 2014; Guerin et al., 2014; Wu et al., 2015). However, this technology is still in development and is not sufficiently mature for routine and repeated use in a large group of subjects, as demanded in a project like the HCP. We have, therefore, opted for an alternative passive B_1^+ shimming approach, which has been shown to locally improve B_1^+ transmit efficiency, with practically no detrimental impact on SAR or image quality (Haines et al., 2010; Teewisse et al., 2012). The approach involves careful placement of 5 mm thick, high permittivity dielectric pads under the neck and on both sides of the head to improve the normally poor B_1^+ in the cerebellum and temporal lobes. These pads consist of a 3:1 mass ratio suspension of calcium titanate powder in water chosen for its high relative permittivity ($\varepsilon_r \approx 110$), chemical inertness and non-toxic properties. Pads made with other materials (i.e. barium titanate) have been shown to further improve transmit efficiency (Teewisee et al., 2012). However due to the toxicity of such substances and the high volume of subjects to be scanned, out of abundance of caution the HCP chose to evaluate only calcium titanate pads. For evaluation, a subject was scanned using actual flip angle imaging (AFI; Yarnykh et al., 2007) and the dMRI protocol with and without pads. Figure 5 shows the effect of the dielectric pads on B_1^+ (quantified by flip angle; top row) and image quality (bottom row). Without the pads, flip angles in the cerebellum are ~1/4th of the nominal flip angle resulting in exceptionally low signal/tissue contrast in the cerebellum. With the pads, flip angles in cerebellar regions increased on average by a factor of 2, corresponding to a 4-fold increase in image SNR, relative to acquisition without pads. Similar effects were also found in the temporal lobes (not shown). The pads do not improve B_1^+ heterogeneities over the entire head and, as such, are not a universal solution as would be pTx pulse design; however, they were useful, as shown in Figure 5, in mitigating signal drop out in the cerebellum and temporal lobes

Overview of the final dMRI protocol

The final dMRI protocol at 7 T for the WU-Minn HCP was determined after extensive piloting on various aspects of the acquisition, key subsets of which have been described above. The HCP dMRI scans utilize the monopolar scheme (Stejskal and Tanner, 1965) within a single-shot, 2D spin-echo multiband EPI acquisition. A multiband factor of 2 and a controlled aliasing PE shift of FOV/2 (Setsompop et al., 2012), a partial Fourier factor of 6/8 with zero filling and an in-plane acceleration of 3 were decided upon and are employed. No special hardware was used to minimize eddy currents other than gradient pre-emphasis, implemented by the vendor in the latest SC72D gradient set. Nominal spatial resolution as measured by voxel dimension (with greater PSF on the image phase encoding axis) is 1.05 mm isotropic (FOV PE × Readout = 210 × 210 mm^2, matrix size PE × Readout = 200 × 200), with 132 slices acquired in interleaved order without gaps to cover the entire brain, including the cerebellum. The 1.05 mm dimension as opposed 1.00 mm arises because of the need to avoid mechanical resonances in the SC72D gradient set. These resonances also imparted a disadvantage to higher spatial resolutions such as 0.8 or 0.9 mm isotropic in this set up. Phase encoding is applied along the anterior-posterior (AP/PA) direction. In the EPI echo train, a total of 50 echoes are collected, with an echo spacing of 0.82 ms and a readout bandwidth 1388 Hz/Pixel, resulting in a total echo train length of 41 ms. As previously described, low SAR fat saturation (Ivanov et al., 2010) was achieved within the aligned-echo variant of the time-shifting MB technique employed (with 1920 μs shift; Auerbach et al., 2013) since the method relies on different bandwidth pulses for excitation and refocusing. Time-shifted MB pulses were generated using vendor optimized apodized sinc RF pulses and were used for excitation and refocusing with individual pulse durations empirically set to 5120 μs and 10240 μs (consistent with the vendor suggested, low SAR, high field settings), with an RF bandwidth time product (BWTP) of 3.2 and 5.2, respectively. The use of the time-shifted pulses also minimized both peak power and online SAR overestimation, as previously described. The refocusing pulse selects slices ~15% thicker than those excited by the excitation pulse to avoid the spin echo slice thinning effect due to imperfect RF slice profiles. Flip angles are nominally set to 90 and 180 degrees, respectively. To avoid excessive overflipping (i.e. greater than 180 degrees) in the center of the brain, while minimizing B_1^+ dropout in the periphery, AFI maps are acquired (Yarnykh 2007) on a per subject basis. Based on this, the reference voltage is set to achieve no greater than 15% over the nominal flip angle in the center of the brain and no greater than 235 volts to keep within SAR limits (Ugurbil et al., 2013). The interleaving slice order minimizes slice crosstalk. Finally, no filtering or interpolation is applied in k-space or image space.

Sampling in q-space includes 2 shells (b= 1000 and 2000 s/mm^2; with diffusion times Δ = 34.0 ms and δ = 14.3 ms, and G_{max} = 69.5 mT/m after vendor supplied gradient duty cycle optimizations are taken into account). Unlike the HCP 3 T protocol, a third shell of b = 3000 s/mm^2 was not used given the longer TR and shorter scan time allocated to dMRI at 7 T. Small b-value variations, due to the cross-terms between diffusion and imaging gradients are calculated (vendor supplied algorithm) in increments of 5 s/mm^2, before gradient nonlinearity correction (Sotiropoulos et al., 2013b). TE and TR are matched across shells (TE = 71 ms, TR = 7.0 s), which are interleaved during acquisition. A total of 286 volumes are acquired. For each shell, 143 data points are obtained, corresponding to 64 unique diffusion gradient directions acquired twice and 15 b=0 volumes, with the phase encoding direction reversed for each pair (i.e. AP and PA pairs). The crusher gradients applied during the so called "b=0" image acquisition are slightly increased to reduce ghosting artifacts (effective b-value increased from 15 to 60 s/mm^2). Directions of the b-vectors (as well as the crusher gradients) are optimized within and across shells (i.e. staggered) to facilitate estimation of eddy current distortions and maximize angular coverage using the approach of Caruyer et al., 2013; http://www.emmanuelcaruyer.com/q-space-sampling.php. In total, 128 non-collinear directions for each PE direction are acquired. Total scanning time for whole brain coverage is ~40 min. To minimize frequency drifts due to the long EPI scan, we split the dMRI acquisition into 4 segments of roughly 10 min (about 71 dMRI volumes) each (Glasser et al., 2013). For each acquisition segment, the resonance frequency is recalibrated. A similar acquisition would take 2 to 3 times longer with conventional 7 T methods and scanners, whilst also having much less SNR due to B_1^+ inhomogeneity and motion sensitivity.

The slice accelerated multiband scanning approach with virtually all of the sequence/reconstruction optimizations described above will be available in the public release of MB acquisition/reconstruction software available from CMRR, including an update enabling greater than 128 slices for high resolution whole brain coverage (see http://www.cmrr.umn.edu/multiband/).

Data Processing

All subjects included in the 7 T HCP scanning protocol were previously scanned at the 3 T with the HCP 3 T protocol. Because of this, time was not allocated for extensive anatomical imaging at 7 T, and, for these subjects, all data were registered to anatomical images obtained at 3 T. In order to evaluate both 3 T and 7 T dMRI data, distortion correction was applied separately to the 3 T and 7 T data prior to further processing using the standard HCP dMRI pipeline (Sotiropoulos et al., 2013b, Glasser et al., 2013). Briefly, phase encoding direction reversed b=0 pairs were used to estimate the susceptibility-induced EPI distortions (Andersson et al., 2003). The estimated off-resonance field was then fed into a Gaussian-Process based framework (Andersson & Sotiropoulos, 2015ab) that estimated the eddy-current induced field inhomogeneities and head motion for each image volume. All these distortions were corrected in a single resampling step using spline interpolation. The corrected diffusion data were then registered to the 3 T native structural space using boundary-based registration (Greve & Fischl, 2009). A rigid body transformation was used for the 3 T diffusion data. An affine (as opposed to rigid body) transformation was used for the 7 T diffusion data, to account for small (1–3%) scaling inconsistencies (from variability in manufacturer's gradient calibrations) between scanners. Furthermore, the 3 T native structural space was non-linearly registered to MNI using the HCP structural pipelines (Glasser et al., 2013). Concatenating the two transforms allowed correspondence between 3 T and 7 T diffusion data to standard MNI space.

RESULTS

HCP 3 T vs. 7 T diffusion examples

The 7 T protocol generates unique, very high spatial resolution whole brain dMRI data, which will provide a rich dataset to the neuroimaging community to further improve our understanding of human brain structural connectivity. Since the HCP database will provide both 7 T and 3 T data on each of the 200 subjects that are being scanned at 7 T, analysis of each dataset separately and/or in combination will enable unique opportunities for enhancing our ability to disentangle and characterize additional white matter pathways.

Although the HCP 3 T dMRI protocol has several inherent SNR advantages over the 7 T protocol (larger voxel size, no in-plane undersampling, longer T_2 and T_2*, stronger maximal gradient strength), matched b-value images (of similar b-vector direction) are actually comparable in terms of image quality and SNR (Figure 1). This is in part due to the 2.3 times higher field strength, the shorter TE (71 vs. 89 ms), and longer TR (5.5 vs. 7 s) of the 7 T data (Ugurbil et al., 2013). Moreover, despite having half the number of q-space samples of the 3 T data, the 7 T data exhibits a number of interesting features in fractional anisotropy (FA) and DTI principal direction of diffusion (PDD) maps (Basser et al., 1994). Figure 6 compares FA-weighted PDD maps from the HCP 3 T (1.25 mm) and 7 T (1.05 mm) from the same volunteer. Both data sets show striking amounts of detail, though the lower resolution of the 3 T data is apparent. Upon closer inspection, it becomes clear that the higher spatial resolution of the 7 T data provides excellent detail including bands of low FA along the gray-white matter borders (Figure 7B), typically seen in ex-vivo samples (Miller et al., 2011; Leuze et al., 2014), and also reported in zoomed dMRI studies with partial brain coverage (Heidemann et al., 2012). Given the gray-white matter boundary (red line; determined from the HCP 3 T T1w structural shown in Figure 7A) it can be seen that the dark bands of FA lie predominantly in the deepest layers of gray matter, along the gray-white matter boundary. By overlaying the PDD over the FA (Figure 7C), it can be seen that these dark bands tend to be strongest along sulcal banks where the PDD depict white matter tracts turning sharply into cortex and weakest in the portions of gyral crowns where the white matter tracts continue straight into the gray matter (red arrows). For improved visualization and to match the resolution of the structural, the diffusion data shown in Figure 7 were upsampled to 0.7 mm isotropic resolution using sinc interpolation prior to DTI analysis.

Figure 8 compares a zoomed in coronal view of PDD overlaid onto FA maps from both the HCP 3 T (left) and 7 T (right). Higher spatial resolution at 7 T, with consequent reduction of partial volume effects, enables visualization of the white matter orientations making sharp turns into cortex, which are more difficult to see in the 3 T data. As a result, the 7 T data also recovers FA in several gray matter regions (yellow circles), which may help to minimize the strong gyral bias in tractography analyses that are found even in the relatively high resolution 3 T HCP diffusion data (Van Essen et al., 2014; Van Essen et al., 2013), as recently shown in (Sotiropoulos et al., 2015ab). To avoid non-monoexponential decay complications (Jbabdi et al., 2012) the comparisons in Figure 8 were made using only b=0 and b=1000 images (including b=2000 and 3000 images resulted in almost identical results but with much more pronounced artifactual bridging of opposing sulcal banks; not shown).

To compare how well long-range connections can be estimated from the 3 T and 7 T dMRI data, first, fiber orientations were estimated for each dataset using multi-shell parametric spherical deconvolution (Jbabdi et al., 2012). The fiber orientation distribution function (fODF) at each voxel was estimated using a Bayesian framework (Behrens et al., 2007). The number of the fODF modes was determined using automatic relevance determination. The deconvolution kernel uses a Gamma distribution of diffusivities to map a single fiber orientation to the diffusion signal and therefore allow multi-exponential decay in b-space (Jbabdi et al., 2012). The likelihood model accounts for the Rician nature of the MRI signal, which is ensured by the SENSE1 image reconstruction of the raw diffusion data (Sotiropoulos et al., 2013c). The fODFs and their uncertainties were then used to estimate long-range connections using probabilistic tractography (Behrens et al., 2007). Tractography seed masks were defined in MNI space, and binning of the estimated path spatial distributions was performed in the same MNI space for both 3 T and 7 T datasets.

Fiber orientation estimation performance averaged across four representative subjects is summarized in Figure 9. As expected given the higher angular resolution at 3 T (greater number of samples and addition of the b=3000 shell), the dispersion (or uncertainty; Figure 9 top) of fiber orientations is typically greater in the HCP 7 T data than in the 3 T data ($p<0.05$, t-test $df=6$). Percent volume of white matter estimated to contain fibers (Figure 9 middle) is similar across 3 T and 7 T data for 1st and 2nd fibers, while the 3 T data is able to detect a significantly greater volume of complex 3rd fiber crossings ($p<0.05$). Density of fibers quantified as number of voxels per ml (Figure 9 bottom) shows the resolution advantage of the HCP 7 T data for 1st ($p<10^{-10}$) and 2nd fibers ($p<0.0005$), while the density of 3rd fibers is similar but tending to be better in the 3 T data ($p=0.12$). The importance of this ~40% improvement in density of 1st and 2nd fiber orientation estimations at 7 T is demonstrated in the tractography examples presented below. These results were derived from and consistent across individual white matter tracts tested (middle cerebellar peduncle, splenium of corpus callosum, superior longitudinal fasciculus, and posterior corona radiate – as identified by the JHU ICBM-DTI-81 white-matter labels atlas; Mori et al., 2004).

A comprehensive comparison of the 7 T and 3 T dMRI tractography is not undertaken in this paper. However, preliminary comparisons demonstrated cases where 7 T HCP data clearly outperformed the 3 T data and other cases where 7 T produced inferior results. Figure 10 (top row) illustrates the acoustic radiations estimated using probabilistic tracktography between the medial geniculate nucleus of the thalamus (seed mask) and the primary auditory cortex (waypoint mask). Both datasets support the estimation of this projection, but the 7 T data allow a thinner, more direct and clear projection to be reconstructed. Generating the same plots but with lower statistical thresholds (bottom row) shows that the 3 T data, in general, has disproportionately more false positive and spurious connections relative to the 7 T data.

Figure 11 shows another thin connection, between subgenual white matter (seed mask) and the amygdala (waypoint mask). The 3 T data find this connection, but they include some false positives with connections going through the fornix/cingulum. The 7 T data do not show this behavior, but paths struggle to reach the amygdala as they traverse regions where B_1^+ field is weak due to profound B_1^+ inhomogeneities. For these subjects, it is in fact possible to fuse the 3 T with the 7 T dMRI data when estimating fiber orientations in a joint analysis. This was done for the data shown in Figure 11 using the RubiX model (Sotiropoulos et al., 2013a), with the estimated paths showing reduced false positives (as in the 7 T data), as well as a strong projection to the amygdala (as in the 3 T data). Additional benefits of simultaneously analyzing datasets from different HCP scanners (i.e. 3 T and 7 T) have been recently illustrated in greater detail (Sotiropoulos et al., 2015ab).

Finaly, Figure 12 shows the sagittal plane of preliminary gray-matter seeded tractography examples (visualization performed in FEI's Amira, Hillsboro, Oregon). Due to the thin and tortuous nature of visual cortex (Figure 12A), the lower resolution 3 T data (left) has difficulty finding connections from one bank of the calcarine sulcus to the other as well as ventral and dorsal visual projections. The 7 T data (right) is able to find these connections. The resolution advantage of the 7 T data is also apparent in the motor cortex (Figure 12B right) where connections to pre-motor cortex are found in addition to fuller horizontal connections in general. This is in contrast to the lower resolution 3 T data where the most common connection found is to the corpus callosum and the motor cortex of the other hemisphere (through plane). Insets show tractography overlaid on FA maps in the seeded sagittal slice. The individual seed voxels are highlighted by green crosshairs.

Discussion

We have described recent advances and many aspects of the 7 T dMRI acquisition optimization efforts undertaken by the WU-Minn HCP consortium. These efforts have culminated in the current protocol, which is being applied to HCP subjects at 7 T (over 100 subjects through the end of 2014, and 200 by the end of the Project). Though many of the 7 T specific considerations were discussed and put in context of the resulting diffusion orientation maps and tractography, many of the MR pulse sequence and post-processing related optimizations benefited from the earlier HCP efforts at 3 T and are detailed in Sotiropoulos et al., 2013b and Ugurbil et al 2013.

It is anticipated that there will be substantial interest in the community to adapt the 7 T HCP dMRI protocol to their own scanners. In contrast to the 3 T HCP protocol, the extensive 7 T optimizations were performed on standard commercially available hardware and are generalizable to Siemens 7 T systems and potentially systems from other vendors. However, there will inevitably be subtle differences, even across systems of the same vendor/model, such that careful optimization and validation on a system-by-system basis are recommended. A few key points to consider are presented below.

The phase encoding direction (AP/PA) as well as resolution (1.05 mm) were independently optimized primarily to minimize echo train length and TE, thus maximizing SNR. Due to peripheral nerve stimulation and mechanical resonance (vibrations and acoustic noise) constraints of our whole body gradient system, the selected phase encoding direction and resolution allowed for ~18% shorter echo spacings. However in a head only gradient system, these limitations would not be applicable and significantly shorter TE's as well as echo train lengths should be achievable.

The choice of AP/PA phase encoding for the 7 T HCP, incidentally, complements the RL/LR phase encoding being used for concurrent 3 T HCP scans. Due to T_2* decay weighting of k-space and partial Fourier zero filling, the phase encoding direction for any EPI protocol will exhibit the largest degree of blurring. Thus, the most and least blurred directions will be complementary between the 3 T and 7 T HCP dMRI datasets. Given T_2* values of 40 ms and 25 ms at 3 T and 7 T, respectively (Yacoub et al., 2001), the FWHM of the point spread function along the phase encoding direction is expected to be ~2.38 mm at 3 T and ~1.87 mm at 7 T. Nevertheless, thanks to the higher resolution of the 7 T data, resolution improvements in the form of resolved u-fibers and reduced gyral bias could be seen even in the sagittal plane (Figure 12). This complementary higher spatial resolution is expected to be particularly advantageous when fusing the 7 T data with 3 T data, for example in the RubiX framework (Sotiropoulos et al., 2013a, Sotiropoulos et al., 2015ab).

The 3 T and 7 T HCP dMRI data are not only complementary in spatial resolution but also in angular resolution. Given the lower spatial resolution, longer T_2, stronger custom diffusion gradients, shorter TR, and the longer time allotted to dMRI in the 3 T scanning protocol, a third shell of higher b-value (b=3000) and more q-space samples were afforded which are important for resolving more complex fiber crossing patterns (Sotiropoulos et al., 2013b). However, with the higher spatial resolution achievable at 7 T, biases due to partial volume effects (e.g. gyral bias in tractography) can be greatly reduced (Figure 7, 12 and Sotiropoulos et al., 2015). As suggested by Sotiropoulos et al., 2013a and preliminary results here (Figure 10–12; Sotiropoulos et al., 2015ab), these dMRI datasets, complementary in both spatial and angular resolution, usher the possibility for "best of both worlds" combinations.

All of the advantages present at the 3 T HCP data relative to the 7 T HCP data can be captured completely at 7 T, while retaining and even improving on the 7 T advantages demonstrated here and elsewhere (Sotiropoulos et al., 2015ab), with the use of higher maximal gradients on the 7 T. There is no theoretical or fundamental engineering reason why gradients with maximal gradient strength of 100 mT/m, as employed in the 3 T HCP scanner, or higher cannot be employed at 7 T; they are simply not available currently. In addition, significant gains in the 7 T dMRI data can be achieved by the use of pTx pulses designed for B_1^+ uniformity with concurrent local and/or global SAR (Wu et al., 2013; Wu et al., 2014; Guerin et al., 2014; Wu et al., 2015); improved B_1^+ homogeneity would eliminate spatially specific SNR losses and signal drop out due to transmit B_1 non-uniformity while reduced local and global SAR would permit higher slice acceleration and shorter TRs.

CONCLUSION

With careful optimization of SAR, B_0 and B_1^+ at 7 T, high resolution, high quality, whole brain dMRI is achieved in 20 mins (40 mins for both PE directions). The higher spatial resolution enables visualization of cortical depth dependent anisotropy and FA typically only seen in restricted field of view (i.e. zoomed) dMRI and ex-vivo human studies. Although the HCP 3 T data are being acquired using 100 mT/m gradients and incorporates denser q-space sampling and higher b-values providing higher angular resolution, 7 T HCP data still demonstrate advantages ascribed primarily to the higher spatial resolution achieved. Preliminary results illustrate promising benefits of combining the complementary HCP 3 T and 7 T diffusion data sets and have paved the way for additional methodological development for improving the characterization of anatomical human brain connectivity at high field. Significant further improvements in 7 T dMRI is possible with the use of gradient sets that can generate higher maximal gradient amplitudes and pTx MB RF pulses that can improve B_1^+ homogeneity and decrease SAR, thus increasing temporal efficiency which can then be used for more extensive q-space sampling within the allotted scanning period.

Acknowledgments

The work reported in this article was supported by the Human Connectome Project (1U54MH091657) from the 16 Institutes and Centers of the National Institutes of Health that support the NIH Blueprint for Neuroscience Research and by the Biotechnology Research Center (BTRC) grant P41 EB015894 from NIBIB, and NINDS Institutional Center Core Grant P30 NS076408.

References

Andersson JL, Skare S, Ashburner J. How to correct susceptibility distortions in spin-echo echo-planar images: application to diffusion tensor imaging. Neuroimage. 2003; 20:870–888. [PubMed: 14568458]

Andersson JLR, Sotiropoulos SN. An integrated approach to correction for off-resonance effects and subject movement in diffusion MR imaging. NeuroImage. 2015a in press.

Andersson JLR, Sotiropoulos SN. Non-parametric representation and prediction of single- and multi-shell diffusion-wighted MRI using Gaussian processes. NeuroImage. 2015b in press.

Auerbach EJ, Xu J, Yacoub E, Moeller S, Ugurbil K. Multiband accelerated spin-echo echo planar imaging with reduced peak RF power using time-shifted RF pulses. Magn Reson Med. 2013; 69:1261–1267. [PubMed: 23468087]

Basser PJ, Mattiello J, LeBihan D. MR diffusion tensor spectroscopy and imaging. Biophysical journal. 1994; 66:259–267. [PubMed: 8130344]

Behrens TE, Berg HJ, Jbabdi S, Rushworth MF, Woolrich MW. Probabilistic diffusion tractography with multiple fibre orientations: What can we gain? Neuroimage. 2007; 34:144–155. [PubMed: 17070705]

Breuer FA, Blaimer M, Heidemann RM, Mueller MF, Griswold MA, Jakob PM. Controlled aliasing in parallel imaging results in higher acceleration (CAIPIRINHA) for multi- slice imaging. Magn Reson Med. 2005; 53:684–691. [PubMed: 15723404]

Caruyer E, Lenglet C, Sapiro G, Deriche R. Design of multishell sampling schemes with uniform coverage in diffusion MRI. Magn Reson Med. 2013; 69:1534–1540. [PubMed: 23625329]

Conolly S, Nishimura D, Macovski A, Glover G. Variable-rate selective excitation. Journal of Magnetic Resonance. 1988; 78:440–458.

Eichner C, Setsompop K, Koopmans PJ, Lutzkendorf R, Norris DG, Turner R, Wald LL, Heidemann RM. Slice accelerated diffusion-weighted imaging at ultra-high field strength. Magn Reson Med. 2014; 71:1518–1525. [PubMed: 23798017]

Eichner C, Wald LL, Setsompop K. A low power radiofrequency pulse for simultaneous multislice excitation and refocusing. Magn Reson Med. 2014; 72:949–958. [PubMed: 25103999]

Feinberg DA, Moeller S, Smith SM, Auerbach E, Ramanna S, Gunther M, Glasser MF, Miller KL, Ugurbil K, Yacoub E. Multiplexed echo planar imaging for sub-second whole brain FMRI and fast diffusion imaging. PLoS One. 2010; 5:e15710. [PubMed: 21187930]

Glasser MF, Sotiropoulos SN, Wilson JA, Coalson TS, Fischl B, Andersson JL, Xu J, Jbabdi S, Webster M, Polimeni JR, Van Essen DC, Jenkinson M, Consortium WU-MH. The minimal preprocessing pipelines for the Human Connectome Project. Neuroimage. 2013; 80:105–124. [PubMed: 23668970]

Gomori JM, Holland GA, Grossman RI, Gefter WB, Lenkinski RE. Fat suppression by section-select gradient reversal on spin-echo MR imaging. Work in progress. Radiology. 1988; 168:493–495. [PubMed: 3393670]

Greve DN, Fischl B. Accurate and robust brain image alignment using boundary-based registration. Neuroimage. 2009; 48:63–72. [PubMed: 19573611]

Griswold MA, Breuer F, Blaimer M, Kannengiesser S, Heidemann RM, Mueller M, Nittka M, Jellus V, Kiefer B, Jakob PM. Autocalibrated coil sensitivity estimation for parallel imaging. NMR Biomed. 2006; 19:316–324. [PubMed: 16705632]

Griswold MA, Jakob PM, Chen Q, Goldfarb JW, Manning WJ, Edelman RR, Sodickson DK. Resolution enhancement in single-shot imaging using simultaneous acquisition of spatial harmonics (SMASH). Magn Reson Med. 1999; 41:1236–1245. [PubMed: 10371457]

Guerin B, Setsompop K, Ye H, Poser BA, Stenger AV, Wald LL. Design of parallel transmission pulses for simultaneous multislice with explicit control for peak power and local specific absorption rate. Magn Reson Med. 2015; 73:1946–1953. [PubMed: 24938991]

Haines K, Smith NB, Webb AG. New high dielectric constant materials for tailoring the B1+ distribution at high magnetic fields. J Magn Reson. 2010; 203:323–327. [PubMed: 20122862]

Heidemann RM, Anwander A, Feiweier T, Knosche TR, Turner R. k-space and q-space: combining ultra-high spatial and angular resolution in diffusion imaging using ZOOPPA at 7 T. Neuroimage. 2012; 60:967–978. [PubMed: 22245337]

Ivanov D, Schafer A, Streicher MN, Heidemann RM, Trampel R, Turner R. A simple low-SAR technique for chemical-shift selection with high-field spin-echo imaging. Magn Reson Med. 2010; 64:319–326. [PubMed: 20574987]

Jbabdi S, Sotiropoulos SN, Savio AM, Grana M, Behrens TE. Model-based analysis of multishell diffusion MR data for tractography: how to get over fitting problems. Magn Reson Med. 2012; 68:1846–1855. [PubMed: 22334356]

Johansen-Berg, H.; Behrens, TE. Diffusion MRI: From Quantitative Measurement to In viso Neuroanatomy. Academic Press; 2013.

Keller PJ, Hunter WW Jr, Schmalbrock P. Multisection fat-water imaging with chemical shift selective presaturation. Radiology. 1987; 164:539–541. [PubMed: 3602398]

Larkman DJ, Hajnal JV, Herlihy AH, Coutts GA, Young IR, Ehnholm G. Use of multicoil arrays for separation of signal from multiple slices simultaneously excited. J Magn Reson Imaging. 2001; 13:313–317. [PubMed: 11169840]

Leuze CW, Anwander A, Bazin PL, Dhital B, Stuber C, Reimann K, Geyer S, Turner R. Layer-specific intracortical connectivity revealed with diffusion MRI. Cereb Cortex. 2014; 24:328–339. [PubMed: 23099298]

Miller KL, Stagg CJ, Douaud G, Jbabdi S, Smith SM, Behrens TE, Jenkinson M, Chance SA, Esiri MM, Voets NL, Jenkinson N, Aziz TZ, Turner MR, Johansen-Berg H, McNab JA. Diffusion imaging of whole, post-mortem human brains on a clinical MRI scanner. Neuroimage. 2011; 57:167–181. [PubMed: 21473920]

Moeller S, Yacoub E, Olman CA, Auerbach E, Strupp J, Harel N, Ugurbil K. Multiband multislice GE-EPI at 7 tesla, with 16-fold acceleration using partial parallel imaging with application to high spatial and temporal whole-brain fMRI. Magn Reson Med. 2010; 63:1144–1153. [PubMed: 20432285]

Mori, S.; Wakana, S.; Van Zijl, PCM. MRI atlas of human white matter. Amsterdam, The Netherlands; San Diego, CA: Elsevier; 2004.

Nagy Z, Weiskopf N. Efficient fat suppression by slice-selection gradient reversal in twice-refocused diffusion encoding. Magn Reson Med. 2008; 60:1256–1260. [PubMed: 18956422]

Norris DG, Koopmans PJ, Boyacioglu R, Barth M. Power Independent of Number of Slices (PINS) radiofrequency pulses for low-power simultaneous multislice excitation. Magn Reson Med. 2011; 66:1234–1240. [PubMed: 22009706]

Park HW, Kim DJ, Cho ZH. Gradient reversal technique and its applications to chemical-shift-related NMR imaging. Magn Reson Med. 1987; 4:526–536. [PubMed: 3613953]

Pfeuffer J, van de Moortele PF, Yacoub E, Shmuel A, Adriany G, Andersen P, Merkle H, Garwood M, Ugurbil K, Hu X. Zoomed functional imaging in the human brain at 7 Tesla with simultaneous high spatial and high temporal resolution. Neuroimage. 2002; 17:272–286. [PubMed: 12482083]

Polimeni JR, Bhat H, Witzel T, Benner T, Feiweier T, Inati SJ, Renvall V, Heberlein K, Wald LL. Reducing sensitivity losses due to respiration and motion in accelerated echo planar imaging by reordering the autocalibration data acquisition. Magn Reson Med. 2015

Pruessmann KP, Weiger M, Scheidegger MB, Boesiger P. SENSE: sensitivity encoding for fast MRI. Magn Reson Med. 1999; 42:952–962. [PubMed: 10542355]

Reischauer C, Vorburger RS, Wilm BJ, Jaermann T, Boesiger P. Optimizing signal-to-noise ratio of high-resolution parallel single-shot diffusion-weighted echo-planar imaging at ultrahigh field strengths. Magn Reson Med. 2012; 67:679–690. [PubMed: 21702067]

Rosen BR, Wedeen VJ, Brady TJ. Selective saturation NMR imaging. J Comput Assist Tomogr. 1984; 8:813–818. [PubMed: 6470246]

Setsompop K, Gagoski BA, Polimeni JR, Witzel T, Wedeen VJ, Wald LL. Blipped-controlled aliasing in parallel imaging for simultaneous multislice echo planar imaging with reduced g-factor penalty. Magn Reson Med. 2012; 67:1210–1224. [PubMed: 21858868]

Setsompop K, Kimmlingen R, Eberlein E, Witzel T, Cohen-Adad J, McNab JA, Keil B, Tisdall MD, Hoecht P, Dietz P, Cauley SF, Tountcheva V, Matschl V, Lenz VH, Heberlein K, Potthast A, Thein H, Van Horn J, Toga A, Schmitt F, Lehne D, Rosen BR, Wedeen V, Wald LL. Pushing the limits of in vivo diffusion MRI for the Human Connectome Project. Neuroimage. 2013; 80:220–233. [PubMed: 23707579]

Smith SM, Beckmann CF, Andersson J, Auerbach EJ, Bijsterbosch J, Douaud G, Duff E, Feinberg DA, Griffanti L, Harms MP, Kelly M, Laumann T, Miller KL, Moeller S, Petersen S, Power J, Salimi-Khorshidi G, Snyder AZ, Vu AT, Woolrich MW, Xu J, Yacoub E, Ugurbil K, Van Essen DC, Glasser MF, Consortium WU-MH. Resting-state fMRI in the Human Connectome Project. Neuroimage. 2013; 80:144–168. [PubMed: 23702415]

Sodickson DK, Griswold MA, Jakob PM. SMASH imaging. Magn Reson Imaging Clin N Am. 1999; 7:237–254. vii-viii. [PubMed: 10382159]

Sotiropoulos SN, Jbabdi S, Andersson JL, Woolrich MW, Ugurbil K, Behrens TE. RubiX: combining spatial resolutions for Bayesian inference of crossing fibers in diffusion MRI. IEEE Trans Med Imaging. 2013; 32:969–982. [PubMed: 23362247]

Sotiropoulos, SN.; Jbabdi, S.; Vu, AT.; Andersson, JL.; Moeller, S.; Lenglet, C.; Yacoub, E.; Ugurbil, K.; Behrens, TE. Fusing 3 and 7 Tesla HCP Datasets for Improved Brain Connectivity Analysis. Proceedings of the 23rd Annual Meeting of ISMRM; Toronto, Canada. 2015. p. 562

Sotiropoulos SN, Hernandez-Fernandez M, Vu AT, Andersson JL, Moeller S, Yacoub E, Lenglet C, Ugurbil K, Behrens TE, Jbabdi S. Spherical Deconvolution by Data Fusion: Combining 3 and 7 Tesla Diffusion MRI for Improved Fibre Orientation Estimation. Neuroimage. 2015 (in review).

Sotiropoulos SN, Jbabdi S, Xu J, Andersson JL, Moeller S, Auerbach EJ, Glasser MF, Hernandez M, Sapiro G, Jenkinson M, Feinberg DA, Yacoub E, Lenglet C, Van Essen DC, Ugurbil K, Behrens TE, Consortium WU-MH. Advances in diffusion MRI acquisition and processing in the Human Connectome Project. Neuroimage. 2013; 80:125–143. [PubMed: 23702418]

Sotiropoulos SN, Moeller S, Jbabdi S, Xu J, Andersson JL, Auerbach EJ, Yacoub E, Feinberg D, Setsompop K, Wald LL, Behrens TE, Ugurbil K, Lenglet C. Effects of image reconstruction on fiber orientation mapping from multichannel diffusion MRI: reducing the noise floor using SENSE. Magn Reson Med. 2013; 70:1682–1689. [PubMed: 23401137]

Stejskal EO, Tanner JE. Spin diffusion measurements: spin echos in the presence of a time-dependent field gradient. Journal of Chemical Physics. 1965; 42:288–292.

Strotmann B, Heidemann RM, Anwander A, Weiss M, Trampel R, Villringer A, Turner R. High-resolution MRI and diffusion-weighted imaging of the human habenula at 7 tesla. J Magn Reson Imaging. 2014; 39:1018–1026. [PubMed: 24259421]

Talagala, SL.; Sarlls, JE.; Inati, SJ. Improved temporal SNR of accelerated EPI using a FLASH based GRAPPA reference scan. Proceedings of the 21st Annual Meeting of ISMRM; Salt Lake City, Utah, USA. 2013. p. 2658

Teeuwisse WM, Brink WM, Haines KN, Webb AG. Simulations of high permittivity materials for 7 T neuroimaging and evaluation of a new barium titanate-based dielectric. Magn Reson Med. 2012; 67:912–918. [PubMed: 22287360]

Ugurbil K. Magnetic Resonance Imaging at Ultrahigh Fields. Ieee T Bio-Med Eng. 2014; 61:1364–1379.

Ugurbil K, Xu J, Auerbach EJ, Moeller S, Vu AT, Duarte-Carvajalino JM, Lenglet C, Wu X, Schmitter S, Van de Moortele PF, Strupp J, Sapiro G, De Martino F, Wang D, Harel N, Garwood M, Chen L, Feinberg DA, Smith SM, Miller KL, Sotiropoulos SN, Jbabdi S, Andersson JL, Behrens TE, Glasser MF, Van Essen DC, Yacoub E, Consortium WU-MH. Pushing spatial and temporal resolution for functional and diffusion MRI in the Human Connectome Project. Neuroimage. 2013; 80:80–104. [PubMed: 23702417]

Van Essen, DC.; Jbabdi, S.; Sotiropoulos, SN.; Chen, C.; Dikranian, K.; Coalson, T.; Harwell, J.; Behrens, TE.; Glasser, MF. Mapping connections in humans and nonhuman primates: Aspirations and challenges for diffusion imaging. In: H, J-B.; TE, B., editors. Diffusion MRI: From Quantitative Measurement to In Vivo Neuroanatomy. Elsevier Academic Press; 2014. p. 337-358.

Van Essen DC, Smith SM, Barch DM, Behrens TE, Yacoub E, Ugurbil K, Consortium WU-MH. The WU-Minn Human Connectome Project: an overview. Neuroimage. 2013; 80:62–79. [PubMed: 23684880]

Vaughan JT, Garwood M, Collins CM, Liu W, DelaBarre L, Adriany G, Andersen P, Merkle H, Goebel R, Smith MB, Ugurbil K. 7 T vs. 4T: RF power, homogeneity, and signal-to-noise comparison in head images. Magn Reson Med. 2001; 46:24–30. [PubMed: 11443707]

Vu, AT.; Auerbach, E.; Lenglet, C.; Moeller, S.; Sein, J.; Van de Moortele, PF.; Ugurbil, K.; Yacoub, E. High resolution whole brain diffusion imagining at 7 T for the Human Connectome Project. Proceedings of the 22nd Annual Meeting of ISMRM; Milan, Italy. 2014. p. 1000

Wong, E. Optimized phase schedules for minimizing peak RF power in simultaneous multi-slice RF excitation pulses. Proceedings of the 20th Annual Meeting of ISMRM; Melbourne, Australia. 2012. p. 2209

Wu X, Schmitter S, Auerbach EJ, Moeller S, Ugurbil K, Van de Moortele PF. Simultaneous multislice multiband parallel radiofrequency excitation with independent slice-specific transmit B1 homogenization. Magn Reson Med. 2013; 70:630–638. [PubMed: 23801410]

Wu X, Schmitter S, Auerbach EJ, Ugurbil K, Van de Moortele PF. A generalized slab-wise framework for parallel transmit multiband RF pulse design. Magn Reson Med. 2015

Wu, X.; Vu, AT.; Schmitter, S.; Auerbach, E.; Moeller, S.; Lenglet, C.; Yacoub, E.; Van de Moortele, PF.; Ugurbil, K. Whole brain single shot diffusion weighted EPI at 7 Tesla using parallel transmit multislice mutiband RF pulses. Proceedings of the 22nd Annual Meeting of ISMRM; Milan, Italy. 2014. p. 311

Yacoub E, Shmuel A, Pfeuffer J, Van De Moortele PF, Adriany G, Andersen P, Vaughan JT, Merkle H, Ugurbil K, Hu X. Imaging brain function in humans at 7 Tesla. Magn Reson Med. 2001; 45:588–594. [PubMed: 11283986]

Yarnykh VL. Actual flip-angle imaging in the pulsed steady state: a method for rapid three-dimensional mapping of the transmitted radiofrequency field. Magn Reson Med. 2007; 57:192–200. [PubMed: 17191242]

Highlights

High quality, ~1mm resolution, whole brain dMRI is achieved at 7 T.

B1+, SAR, and motion sensitivity issues are addressed.

High spatial resolution reduces gyral bias in tractography analysis.

Fusion of high angular and high spatial resolution datasets is proposed.

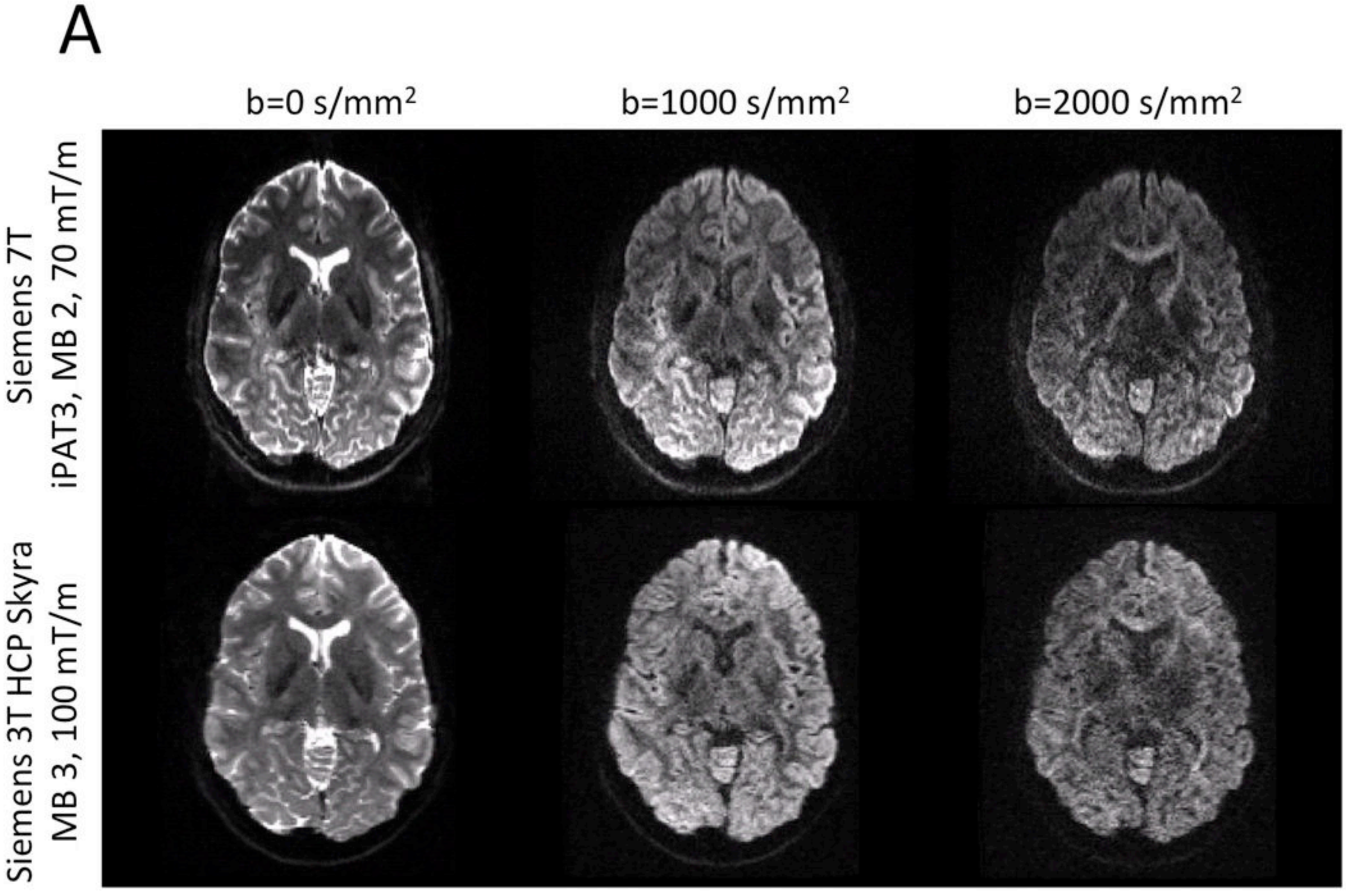
A
b=0 s/mm²
b=1000 s/mm²
b=2000 s/mm²
Siemens 7T
iPAT3, MB 2, 70 mT/m
Siemens 3T HCP Skyra
MB 3, 100 mT/m

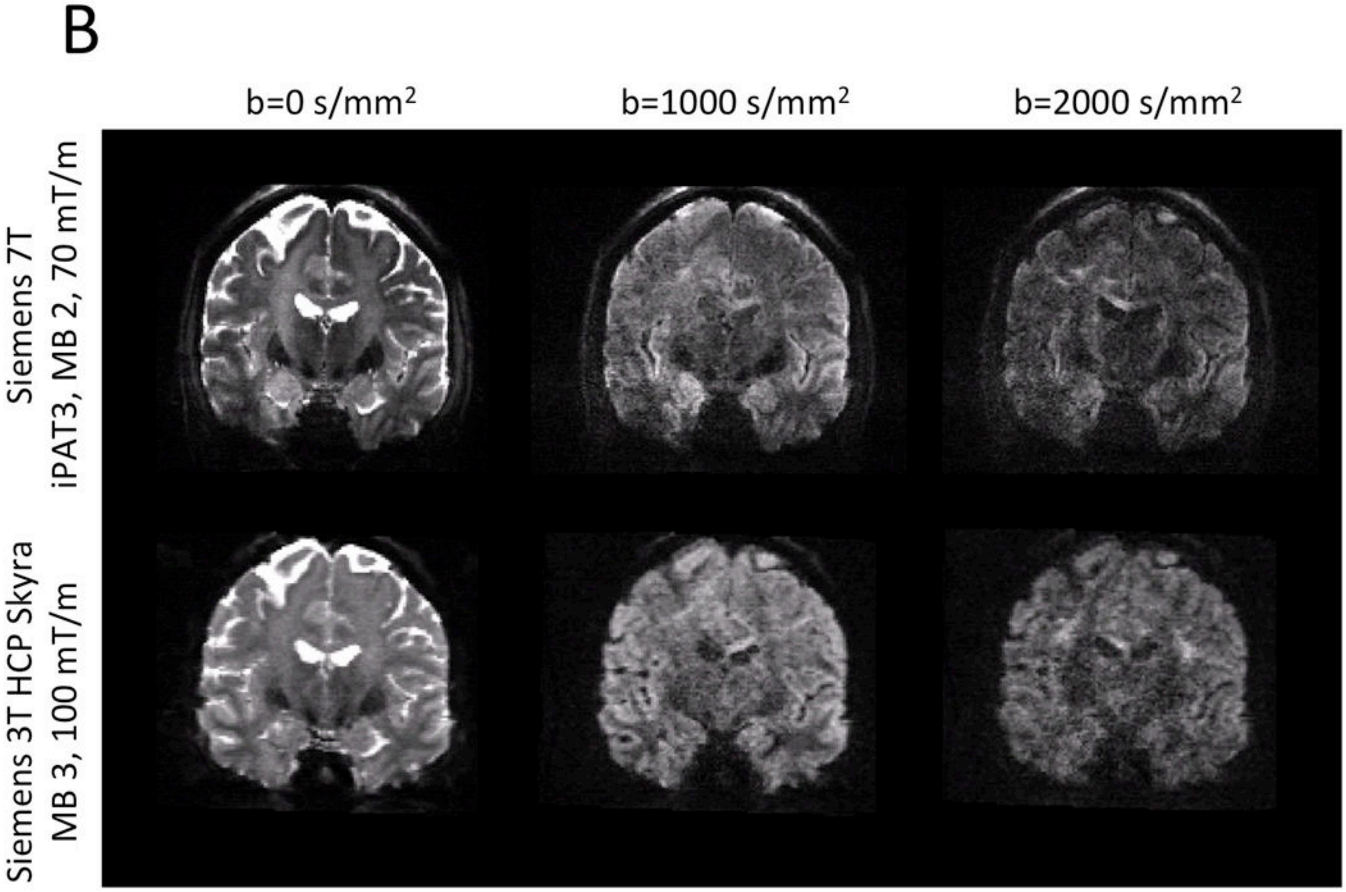
B
b=0 s/mm²
b=1000 s/mm²
b=2000 s/mm²
Siemens 7T
iPAT3, MB 2, 70 mT/m
Siemens 3T HCP Skyra
MB 3, 100 mT/m

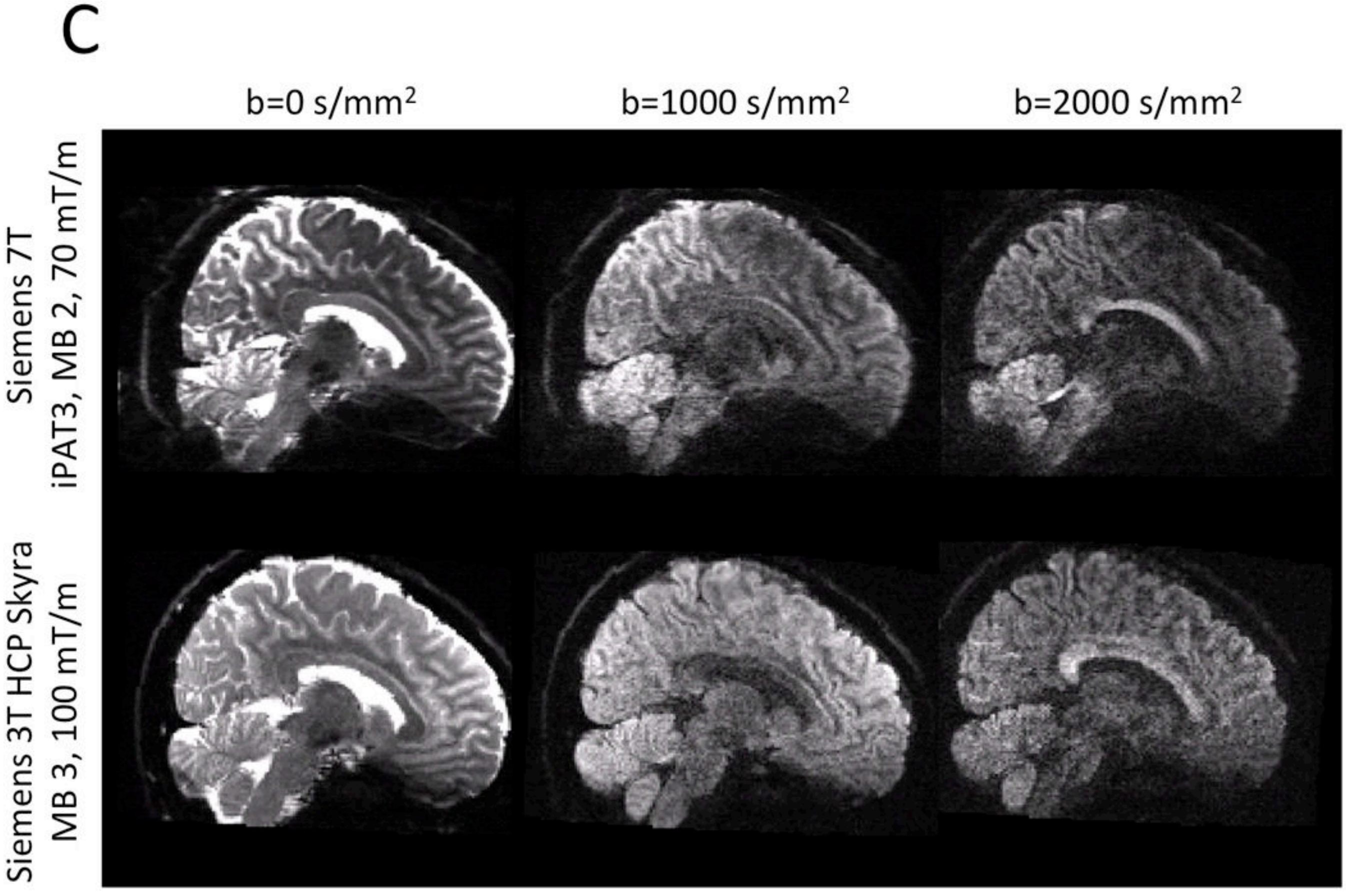

Figure 1.

Representative examples of dMRI from Siemens 7 T and 3 T HCP systems. The resolution advantage of the 1.05 mm 7 T data over the 1.25 mm 3 T data is quite apparent. Image intensities are presented in arbitrary units after distortion correction and averaging across paired phase encoding directions.

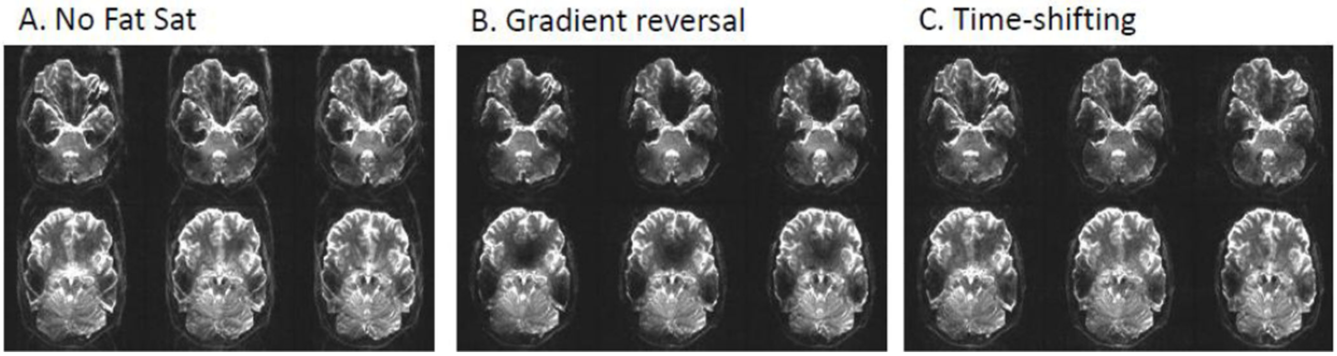

Figure 2.

7 T dMRI b=0 images with various fat saturation options. A) No fat saturation applied. B) Gradient reversal. This is the standard method at 3 T. C) Time-shifting. This is the method employed for the HCP 7 T dMRI protocol.

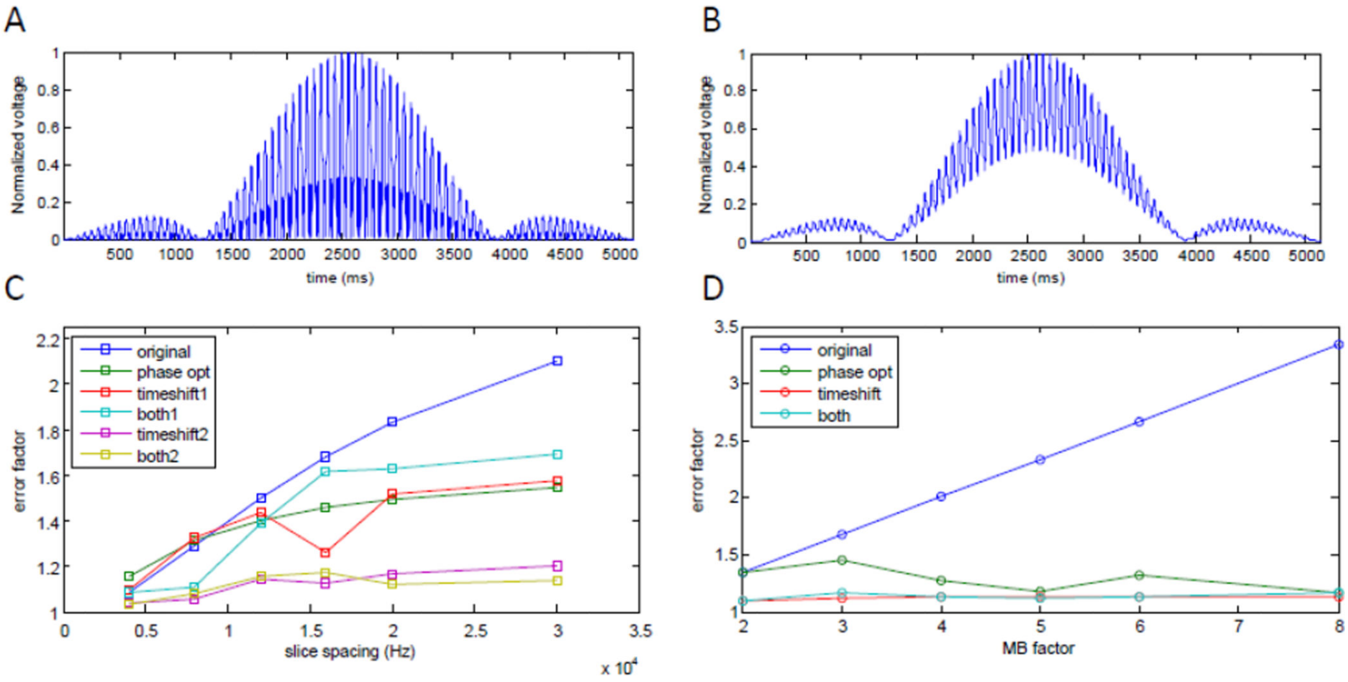

Figure 3.

SAR measurement error simulation. A) Typical MB=3 RF pulse. B) The same pulse as seen by a system with a typical 25 μs decay time constant. In this case, the SAR will be measured to be 168% of the actual SAR (error factor 1.68). C) SAR error factor, for MB=3, as a function of slice spacing. D) SAR error factor as a function of MB factor. Phase optimization of the individual slices comprising the MB RF pulse as well as time shifting both tend to reduce the SAR error factor (time-shift1=1280 μs; time-shift2=1520 μs).

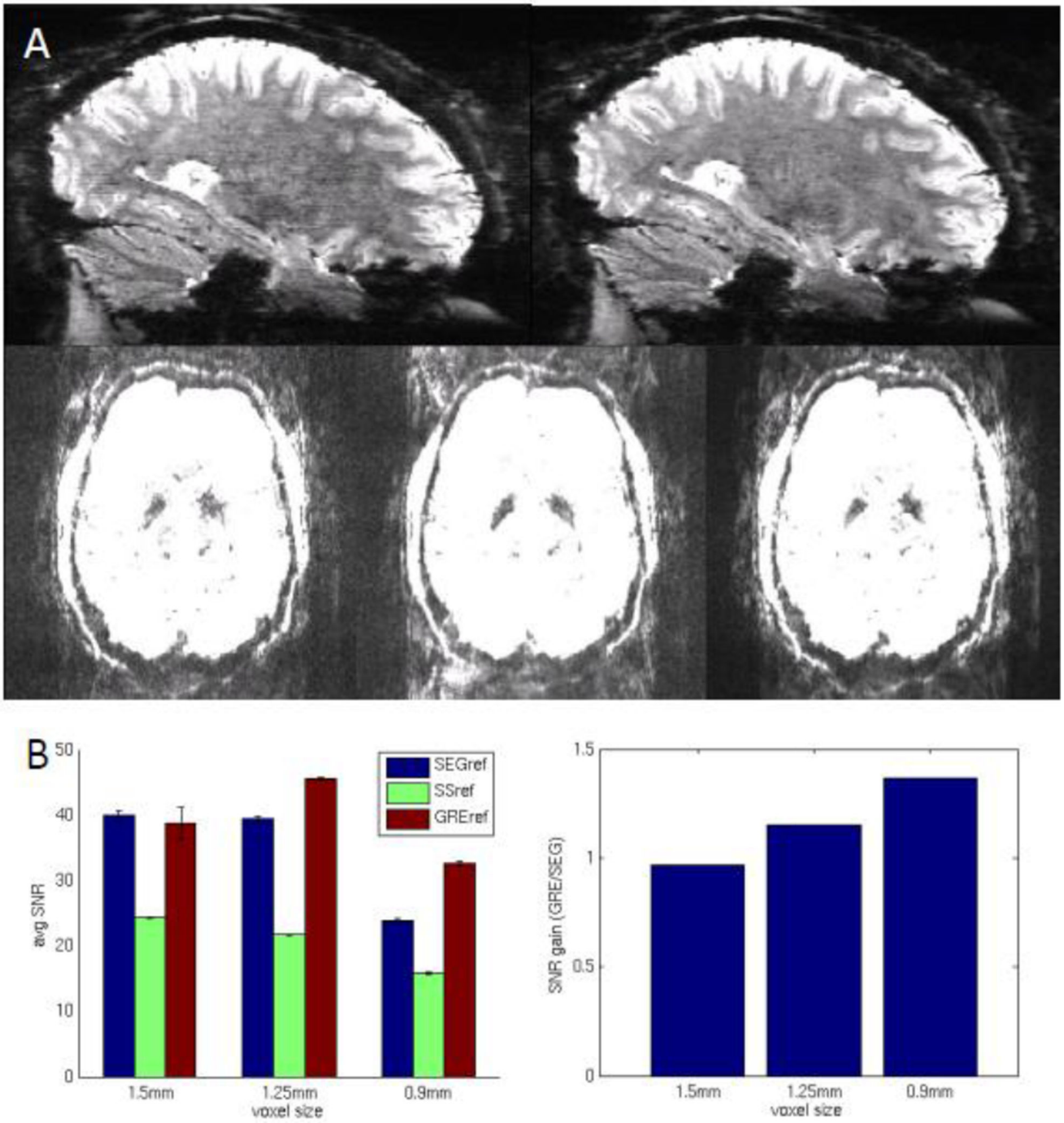

Figure 4.
Evaluation of in-plane acceleration reference scan. A) iPAT=3 MB=3 0.9 mm example GE EPI images. Sagittal cross-sections show degraded image quality using the segmented EPI reference scan (left) versus the GRE reference scan (right). Axial slices show improved image quality using the GRE reference scan (right) versus the single-shot (middle) and segmented (left) EPI reference scans. Images are windowed to aid visualization of artifact and noise levels. B) SNR as a function of image resolution and reference scan (left). The SNR improvement provided by the GRE reference scan increases with resolution (right).

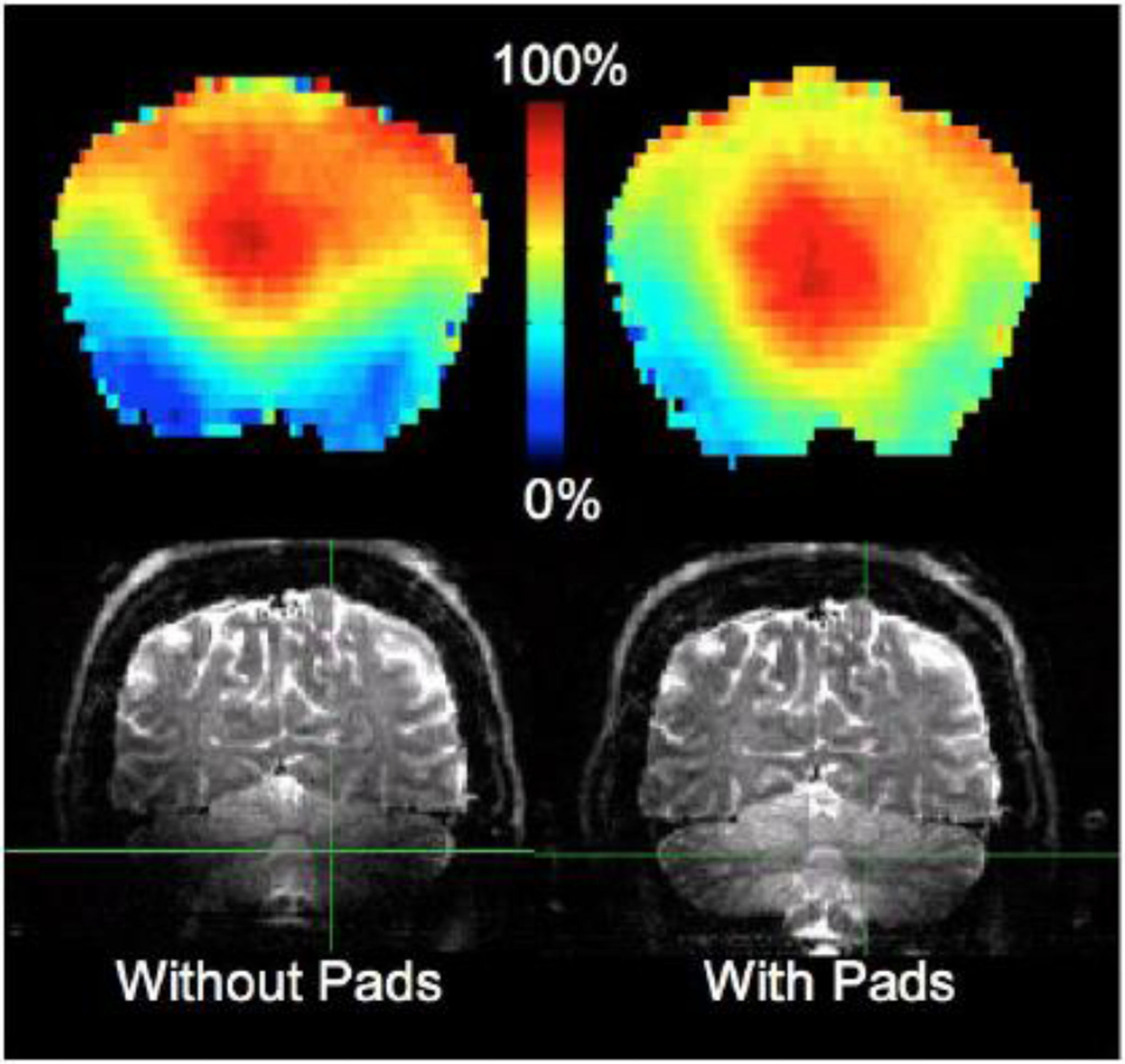

Figure 5.

Effect of the dielectric pads on B_1^+. Flip angle map (shown as percentage of nominal flip angle; top row). Coronal cross section of dMRI b=0 images (bottom row). Without the pads (left) flip angles in the cerebellum are ~1/4th of the nominal flip angle resulting in low signal/tissue contrast in the cerebellum. With the pads (right) flip angles in cerebellar regions substantially increased on average by a factor of 2, corresponding to a 4-fold increase in image SNR.

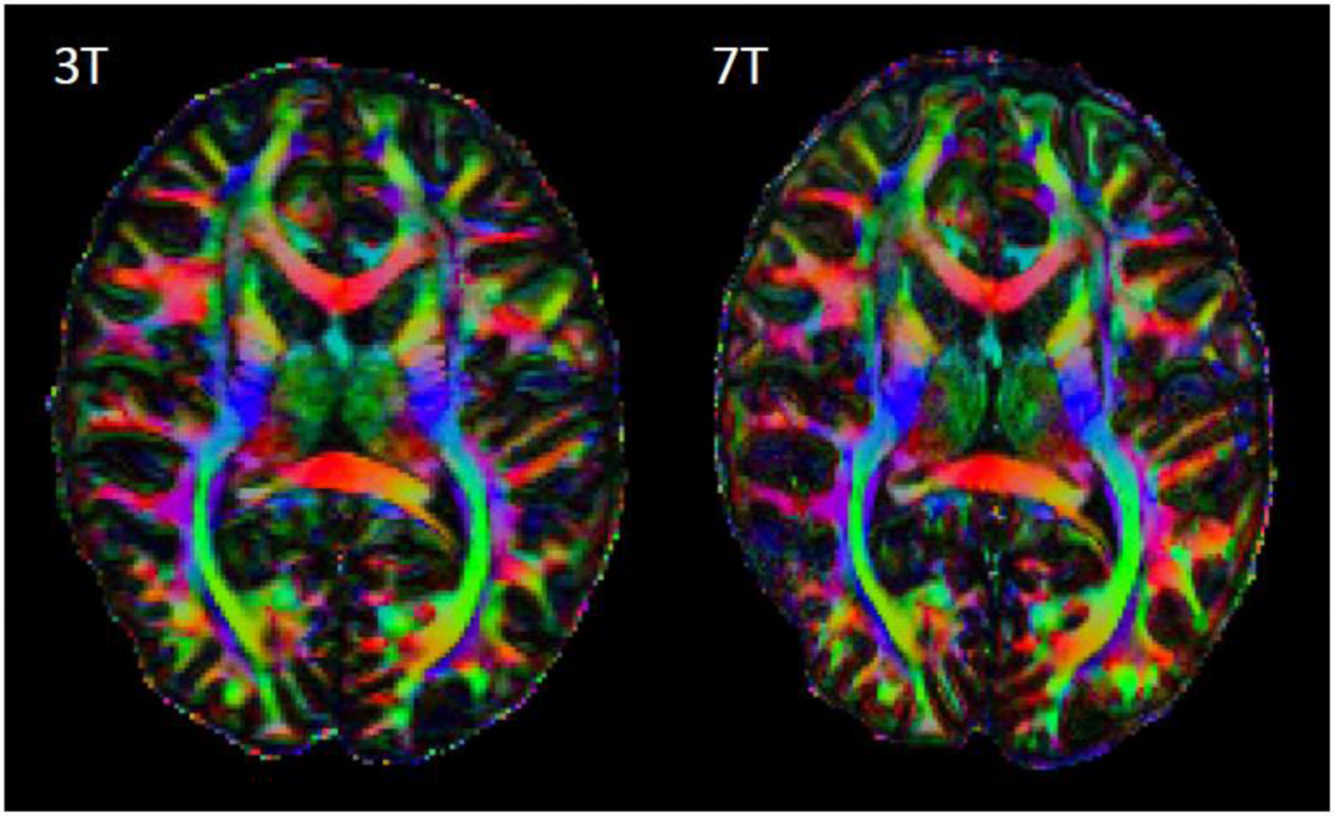

Figure 6.

Color fractional anisotropy (FA) maps from the HCP 3 T (1.25 mm) and 7 T (1.05 mm) from the same volunteer (Colors depict the principal fiber orientation and gray scale intensities are defined by FA).

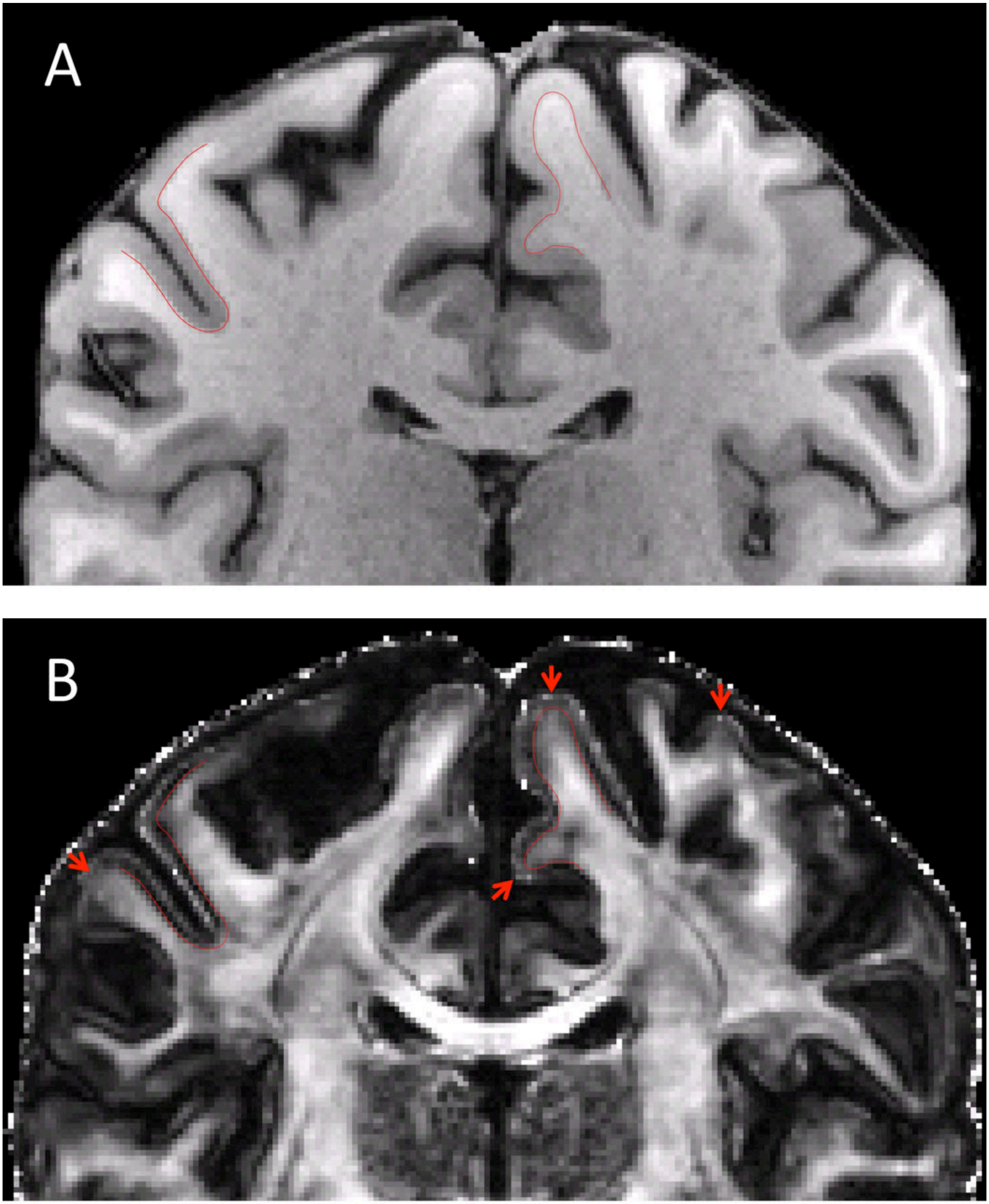
A
B

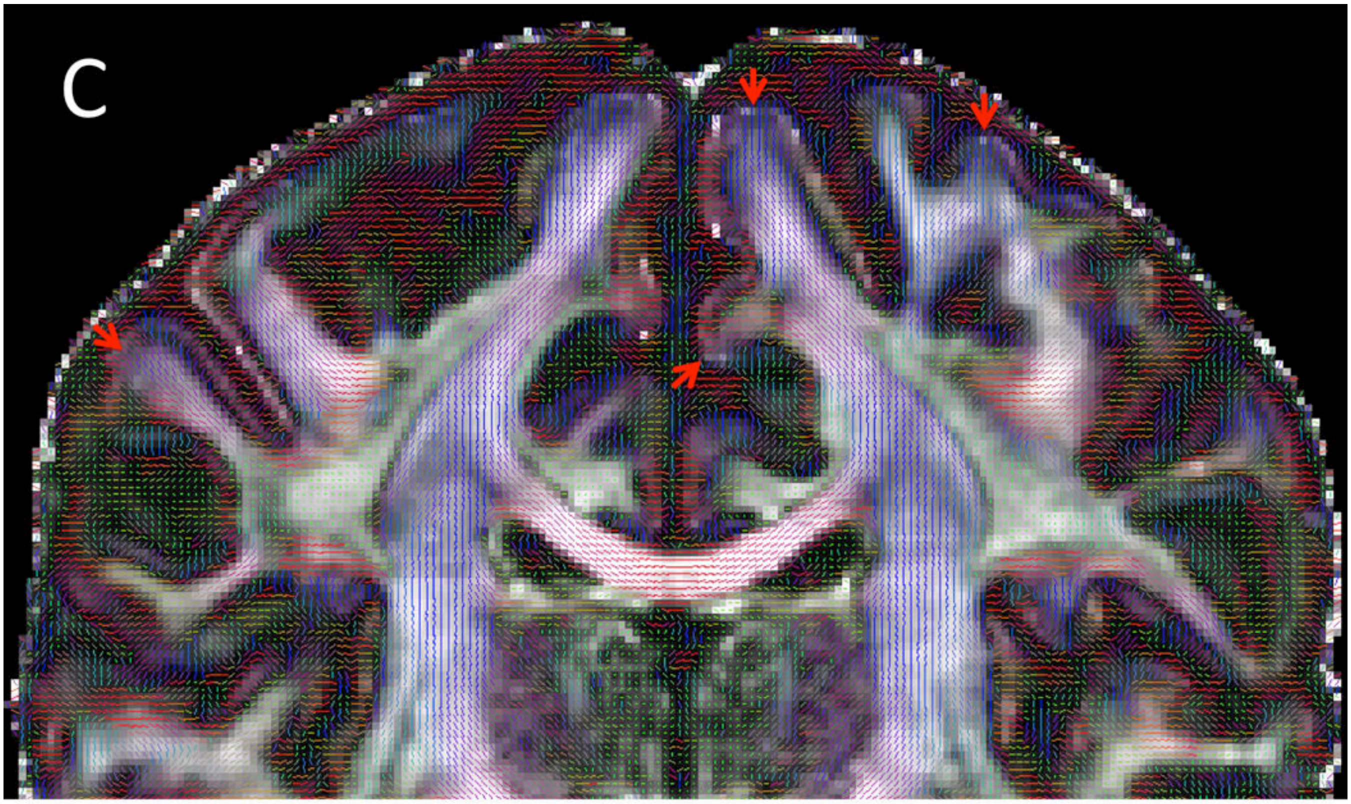

Figure 7.

Cortical diffusion properties. A) T1w structural B) FA map C) PDD map. FA exhibit characteristic dark bands along the gray and white matter boundary. With the gray-white matter boundary determined from the T1w structural (red line), it can be seen that the dark bands lie predominantly in the deepest layers of gray matter. The dark bands of FA tend to be strongest along sulcal banks where the PDD depict white matter tracts turning sharply into cortex and weakest in the portions of gyral crowns where the white matter tracts continue straight into the gray matter (red arrows). For improved visualization and to match the resolution of the T1w structural, the diffusion data here are shown upsampled (using sinc interpolation) to 0.7 mm isotropic resolution.

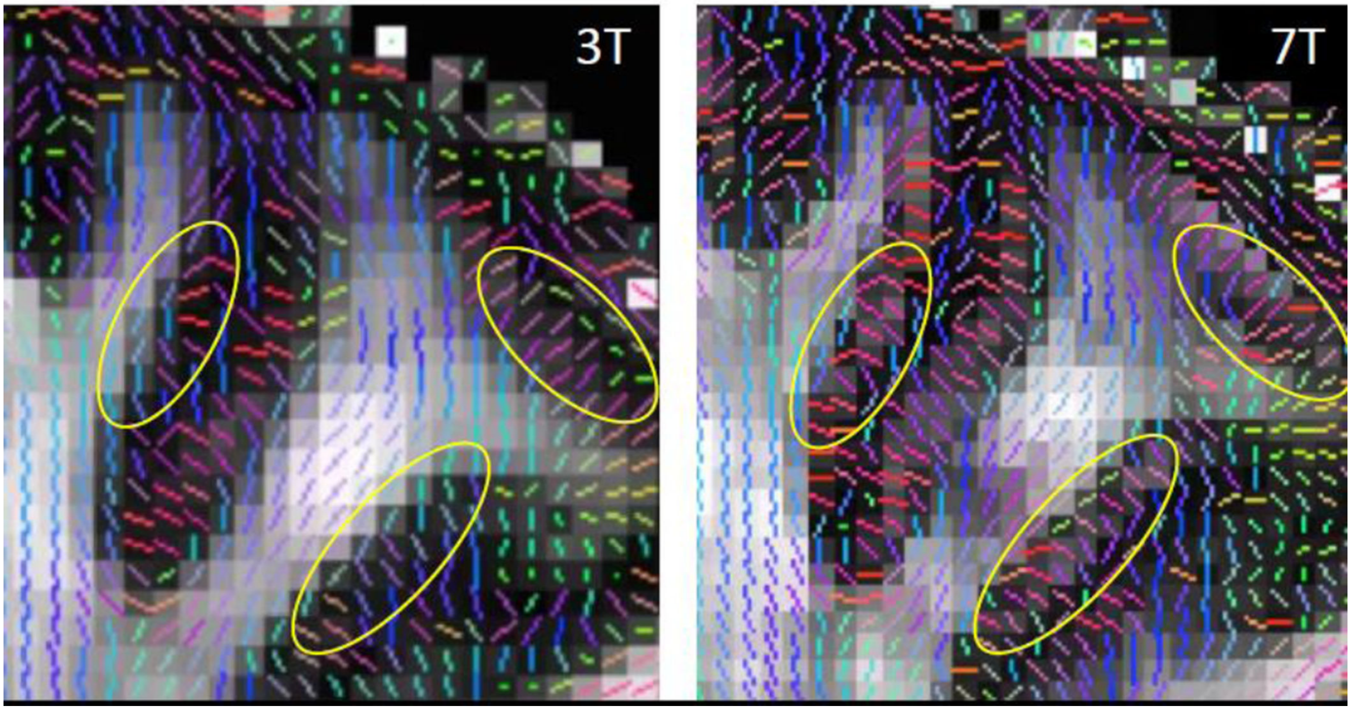

Figure 8.

Zoomed in coronal view of DTI PDD maps overlaid on corresponding FA maps. HCP 3 T (left). 7 T (right). The improvement in spatial resolution at 7 T enables visualization of the white matter orientations making sharp turns into cortex, which are more difficult to see in the 3 T data. Due to the higher resolution and reduced partial volume effects, the 7 T data also recovers gray matter regions of low FA (yellow circles).

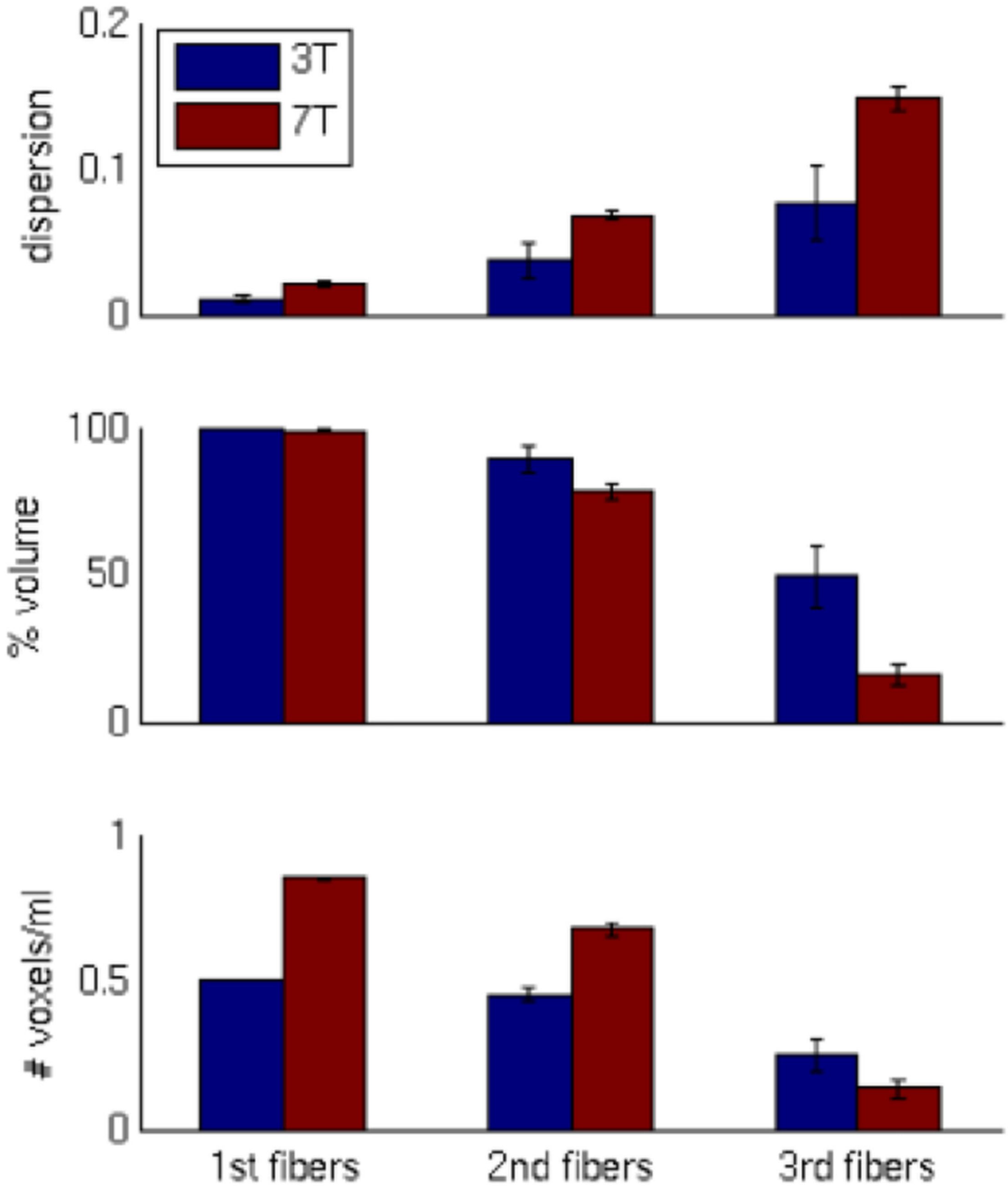

Figure 9.

Fiber orientation estimation performance of HCP 3 T and 7 T data. Dispersion (top) is significantly greater for the 7 T data relative to the 3 T data ($p<0.05$, t-test $df=6$). Percent volume of white matter estimated to contain fibers (middle) is similar across 3 T and 7 T data for 1st and 2nd fibers. However, the 3 T data is able to detect a significantly greater volume of 3rd fiber crossings ($p<0.05$). Density of fibers quantified as number of voxels per ml (bottom) shows the resolution advantage of the HCP 7 T data for 1st ($p<10^{-10}$) and 2nd fibers ($p < 0.0005$), while the density of 3rd fibers is similar, tending to be slightly better in the 3 T data ($p = 0.12$). Errorbars are SEM across the same four subjects.

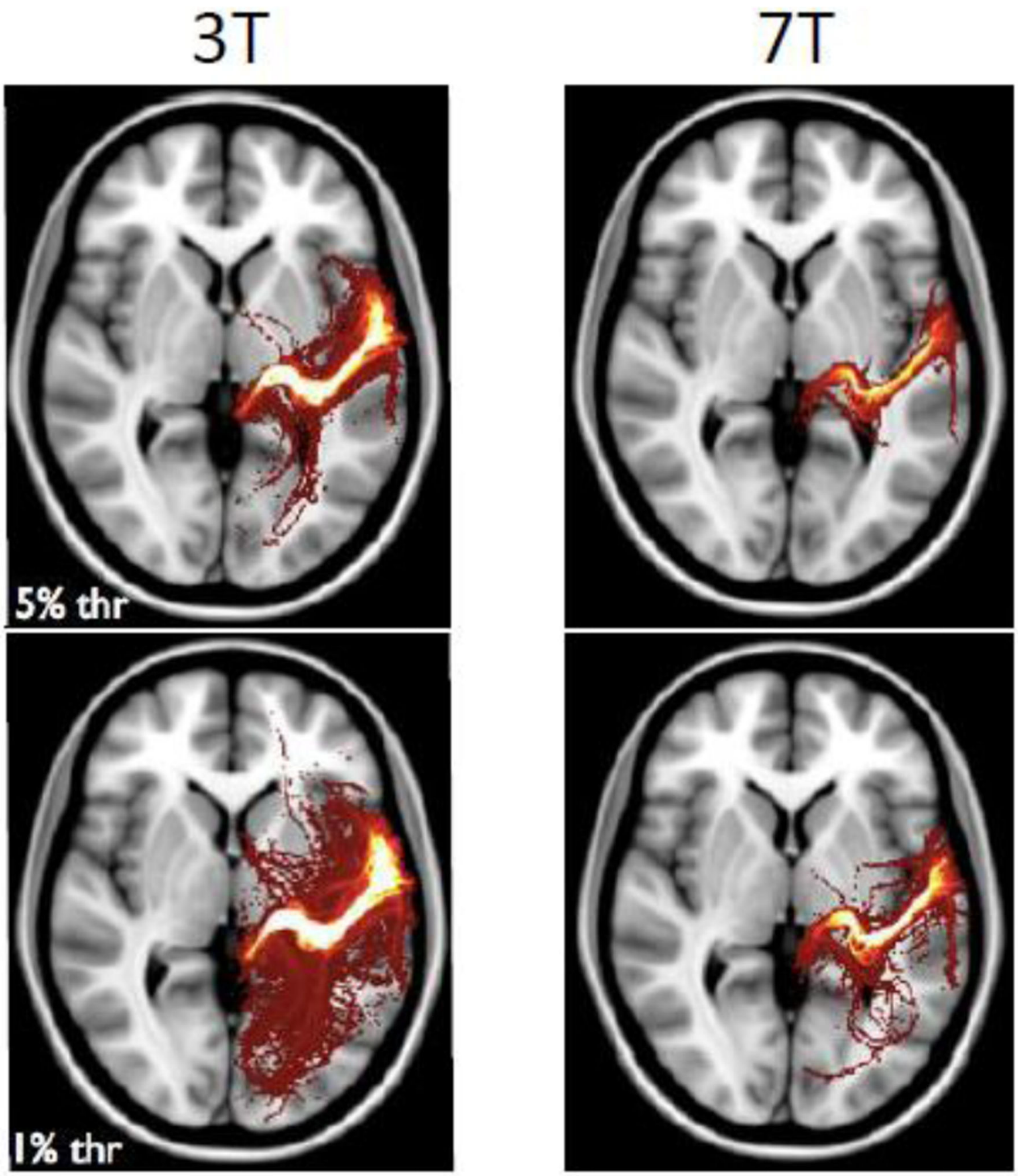

Figure 10.

Probabilistic tractography results between the medial geniculate nucleus of the thalamus and the primary auditory cortex. Both datasets support the estimation of this connection (top row). However, relative to the 3 T data (left), the 7 T data (right) allow a thinner, more direct and clear connection to be reconstructed. Generating the same plots but with lower statistical thresholds (bottom row) shows that the 3 T data, in general, has more false positive and spurious connections relative to the 7 T data.

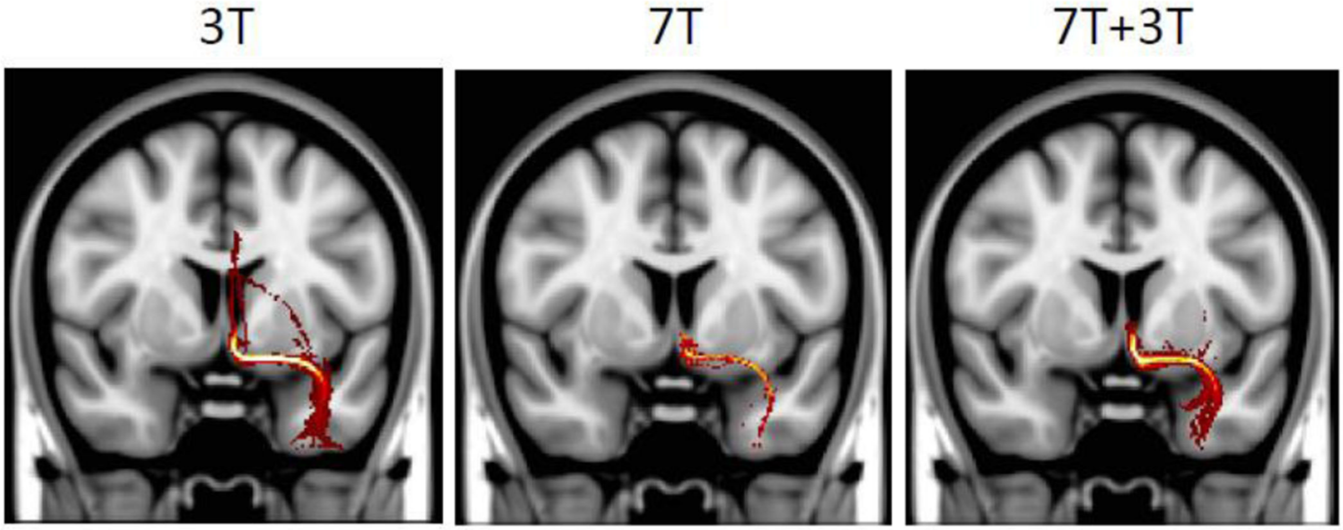

Figure 11.

Probabilistic tractography results between subgenual white matter and the amygdala. The 3 T data (left) find this connection, but include some false positives with connections going through the fornix/cingulum. The 7 T data (middle) have fewer false positives but paths struggle to reach the amygdala due B_1^+ field inhomogeneities and low SNR. By combining the 3 T and 7 T dMRI data using Rubix (right) when estimating fiber orientations, the estimated paths show reduced false positives (as in the 7 T data), as well as a strong projection to the amygdala (as in the 3 T data).

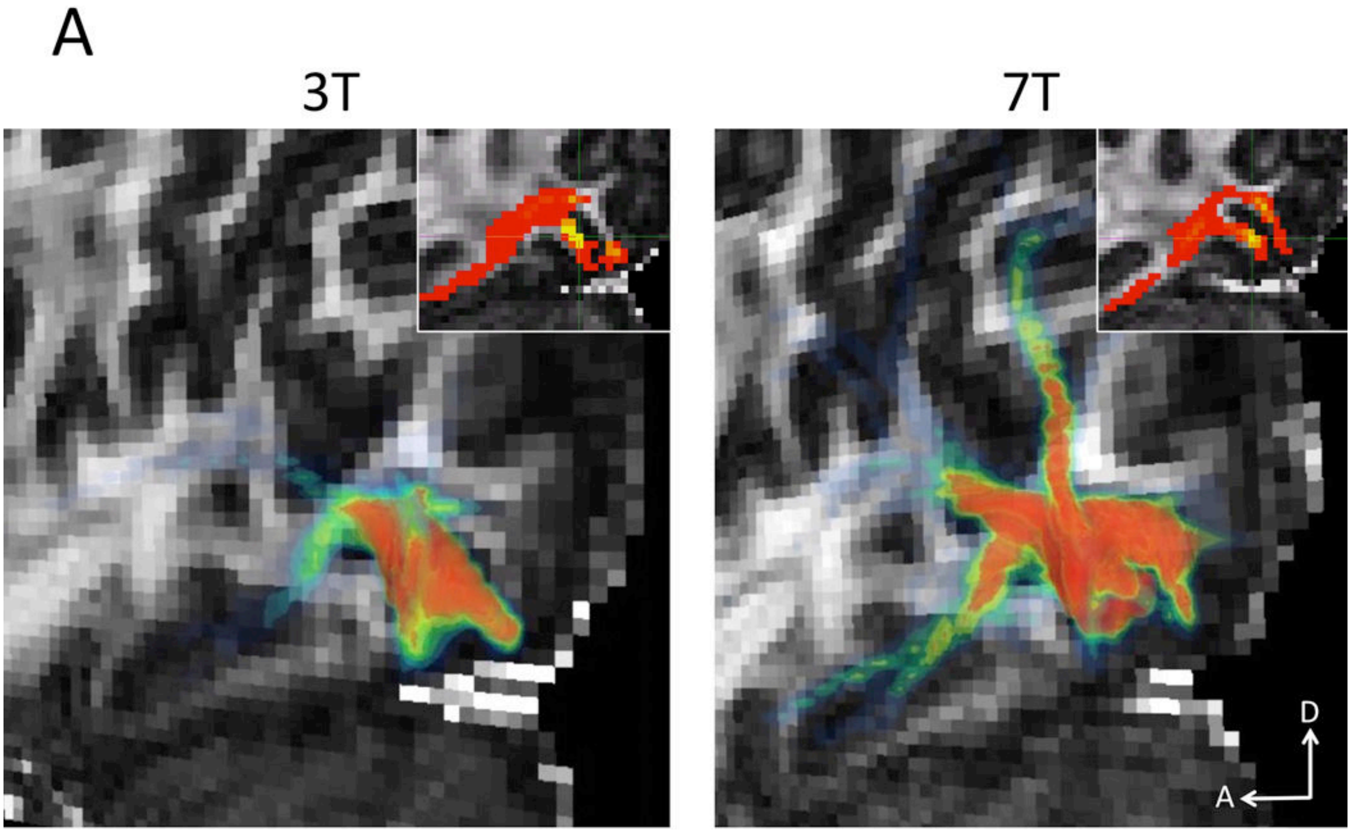
A
3T
7T
D
A

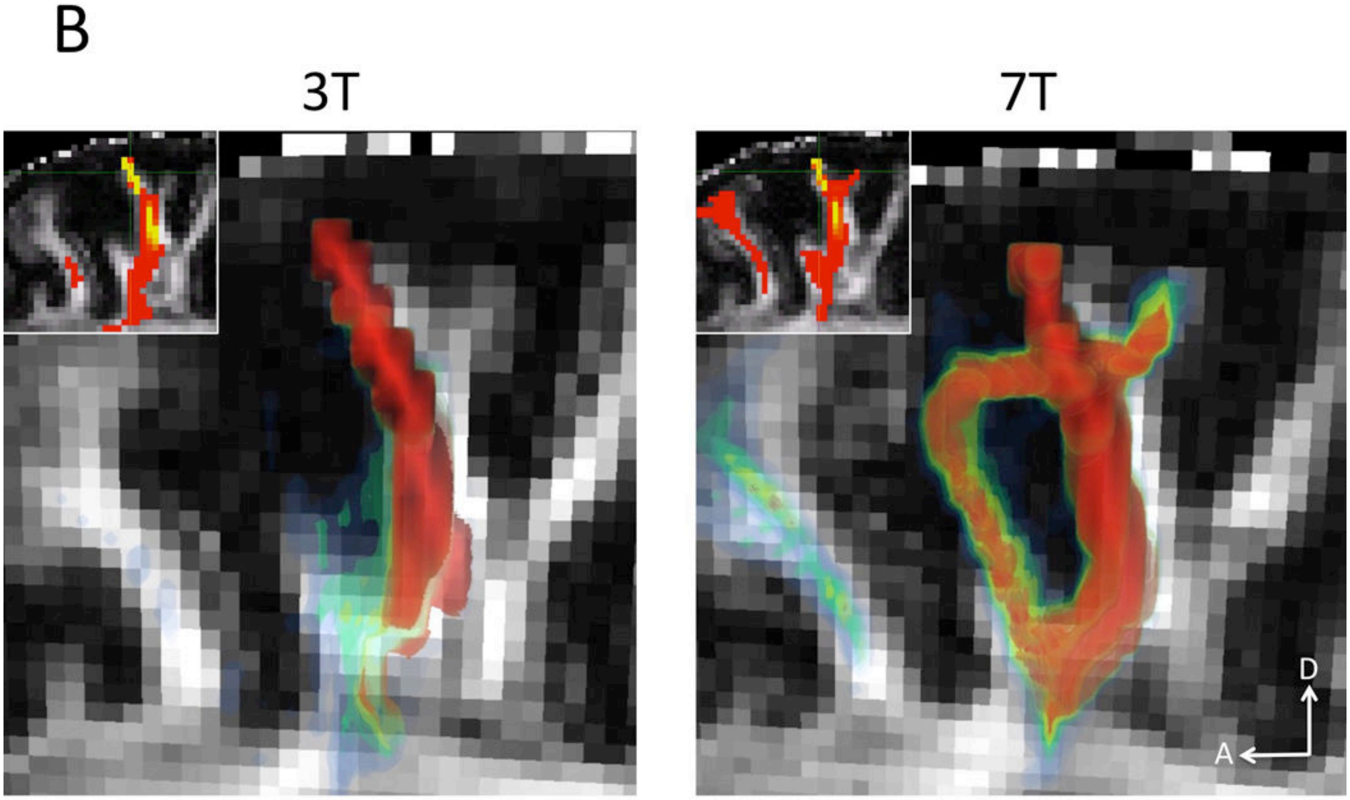

Figure 12.

Gray-matter seeded probabilistic tractography examples. A) Primary visual cortex seed. Due to the thin and tortuous organization of the visual cortex, the lower resolution 3 T data (left) has difficulty finding connections from one bank of the calcarine sulcus to the other as well as ventral and dorsal visual projections. The 7 T data (right) is able to find these connections. B) Primary motor cortex seed. Given the lower resolution of the 3 T data (left), the most common connection found is to the corpus callosum and the motor cortex of the other hemisphere. However, with the higher resolution of the 7 T data, connections from motor cortex to pre-motor cortex are found in addition to fuller horizontal connections in general. Insets show tractography overlaid on FA maps in a sagittal slice. The seed voxels are highlighted by green crosshairs.